BNL-213515-2020-JAAM

Probing Structural Reconstruction of Metal Nanoparticles under Annealing and Water Vapor Conditions: A Theoretical Study

Z. Wang, M. S. Hybertsen

To be published in "The Journal of Physical Chemistry C"

November 2019

Center for Functional Nanomaterials

Brookhaven National Laboratory

U.S. Department of Energy

USDOE Office of Science (SC), Biological and Environmental Research (BER) (SC-23)

Notice: This manuscript has been authored by employees of Brookhaven Science Associates, LLC under Contract No. DE-SC0012704 with the U.S. Department of Energy. The publisher by accepting the manuscript for publication acknowledges that the United States Government retains a non-exclusive, paid-up, irrevocable, world-wide license to publish or reproduce the published form of this manuscript, or allow others to do so, for United States Government purposes.

DISCLAIMER

This report was prepared as an account of work sponsored by an agency of the United States Government. Neither the United States Government nor any agency thereof, nor any of their employees, nor any of their contractors, subcontractors, or their employees, makes any warranty, express or implied, or assumes any legal liability or responsibility for the accuracy, completeness, or any third party's use or the results of such use of any information, apparatus, product, or process disclosed, or represents that its use would not infringe privately owned rights. Reference herein to any specific commercial product, process, or service by trade name, trademark, manufacturer, or otherwise, does not necessarily constitute or imply its endorsement, recommendation, or favoring by the United States Government or any agency thereof or its contractors or subcontractors. The views and opinions of authors expressed herein do not necessarily state or reflect those of the United States Government or any agency thereof.

Probing Structural Reconstruction of Metal Nanoparticles under Annealing and Water Vapor Conditions: A Theoretical Study

Zeming Wang,[†] Wei An,[*,†], Yangang Sun,[†] Mark S. Hybertsen[‡]

[†]College of Chemistry and Chemical Engineering, Shanghai University of Engineering Science, Songjiang District, Shanghai 201620, China

[‡]Center for Functional Nanomaterials, Brookhaven National Laboratory, Upton, New York 11973, United States

*E-mail: weian@sues.edu.cn

ABSTRACT: Understanding the structural reconstruction of metal nanoparticles (NPs) under working conditions is of particular importance to catalytic processes. Here, using Wulff construction combined with density functional theory (DFT) and molecular dynamics (MD) simulation, we investigated truncated octahedron-based Rh and Ir NPs (3.5-, 5.5- and 9.5-nm in size) with different morphology for their structural reconstruction under annealing and water vapor conditions. Our MD results show that the NPs with lower average atomic coordination number ($\overline{CN}$) of surface atoms have lowered structural transformation inertness and thermal stability, resulting in more severe structural transition especially for smaller-sized NPs and Ir NPs. Under water vapor conditions, the competition between the interfacial tension ($\overline{\gamma_{\mathrm{hkl}}^{\mathrm{int}}}$) of (111) and (110) facets plays a major role in driving the shape evolution of Rh and Ir NPs by minimizing the total surface tension. It is revealed that annealing in vacuum/water vapor condition is an irreversible/reversible process on Rh and Ir NPs. We identified that the total adsorbate-metal $\overline{\gamma_{\mathrm{hkl}}^{\mathrm{int}}}$ can serve as a key stability parameter for describing the potential energy surface of adsorbate-metal NP system in a variable gaseous environment (*P*, *T*).

1. INTRODUCTION

Metal nanoparticles (NPs) have received rapidly growing research attention owing to their novel properties suitable for a variety of applications such as catalysis and energy conversion.[1-3] The size, shape, structure and composition are the key parameters that define one NP from another and render them exceptional functionality. Specifically, the morphology of a NP associated with the topography of surface sites (e.g., terraces, steps, edges, kinks and defects) play a critical role in determining activity and selectivity of metal NPs-based catalysts.[4-8] As noble metals, Rh and Ir NPs are known to catalyze a number of important catalytic reactions such as ethanol electro-oxidation in direct ethanol fuel cell (DEFC),[9-10] oxygen evolution reaction (OER),[11-12] steam reforming of methane (SRM),[13] steam reforming of ethanol (SRE),[14-15] reduction of nitrogen oxides (NO_X) in three-way catalysts (TWC),[16] hydrodeoxygenation (HDO) of bio-oils,[17-18] CO hydrogenation[19] and/or oxidation.[20-21] So far, wet-chemical, kinetically-controlled methods[1, 22-23] have realized the controlling of the surface/interfacial structures of metal NPs (including Rh and Ir)[24-25] that exhibit distinct morphology including cubic,[26] cuboctahedron,[27] icosahedron,[22] and tetrahexahedron[28] for catalytic and electrocatalytic applications.

However, the morphology of as-synthesized metal NPs are affected by the external gaseous environment[29-32] that may control and/or induce their atomic-scale growth with specific shape and local structure (e.g., steps/edges) under thermodynamically and kinetically controlled conditions.[28] More importantly, metal nanoparticle catalysts under working conditions are exposed to gaseous (reactive) atmosphere such as H_2O,[33-34] H_2 and O_2,[35-37] CO and NO[38-39] and even N_2[40] under given temperature and pressure that can significantly alter the surface structure of metal NPs (including Rh[20] and Ir[39]). This has led to tremendous complexity that poses a major challenge for illustrating mechanistic aspect of NP's anisotropic growth and shape evolution solely by means of experimental technique. Consequently, theoretical modeling has been commonly evoked to assist the experimental investigation and/or to conduct independent research.[41-49]

Recently, the multi-scale atomistic simulation approach[50] has gone beyond the pristine NP and the extended surface models in vacuum enabling modeling of metal NPs under working conditions with reliable accuracy. For example, Zhu et al.[51] found that the water vapor has different effects on the different metal (Cu, Au, Pt and Pd) NPs and particularly, the water vapor induce the shape evolution of Cu NP dramatically while the structures of Pd and Pt NPs could also be reshaped under certain water

vapor environment. Their findings on shape evolution process of Cu NPs agree well with the experimental observations.[33] On the other hand, the thermal stability of metal NPs is generally of relevance to their technical applications.[52-53] In this regard, simulations of annealing under vacuum conditions can provide valuable information on intrinsic stability of metal NPs by exploring their potential energy surface and structure change as a function of temperature, especially for those synthesized using kinetically-controlled methods.[54-55] In this work, we applied Wulff construction combined with density functional theory (DFT) and molecular dynamics (MD) simulation to investigate Rh and Ir NPs (3.5 nm, 5.5nm, and 9.5 nm in size) under annealing and water vapor conditions, particularly focusing on their thermal stability and size/shape-dependent evolution of atomic structure, which are critical to their catalytic applications.

2. MODELS AND COMPUTATIONAL METHODS

2.1. Nanoparticle Models.

The equilibrium geometry of prototypical Rh and Ir nanoparticles were built using Wulff construction by which the length (h_j) of the vector drawn from the center of a crystal normal to the jth (hkl) facet will be proportional to its surface energy (γ_{hkl}), i.e., $\gamma_{hkl} : h_j = \lambda$, where λ is constant dependent on the environmental media and on the crystal size. A facet with higher surface energy tends to grow farther while a facet with smaller surface energy tends to become dominant for a nanoparticle. With the growth of all the facets of Miller indexes completed, the equilibrium shape of nanoparticle can be constructed with the minimal total surface Gibbs energy. In vacuum, the surface energy of low-index {111}, {100}, and {110} facets of Rh and Ir can be calculated as:[56]

$$\gamma_{hkl} = \frac{1}{2A}(E_{slab} - \frac{N_s}{N_b} E_{bulk}) \quad (1)$$

Where γ_{hkl}, A, E_{slab} and E_{bulk} represent DFT-calculated surface tension and surface area of the exposed (hkl) facet, total energy of the slab (containing N_s atoms) and the bulk (containing N_b atoms), respectively. More positive γ_{hkl} value indicates a less stable surface with higher surface energy.

Under H_2O environment, the surface tension can be modified as:[57]

$$\gamma_{hkl}^{int} = \gamma_{hkl} + \theta\left(\frac{E_{ads}}{A_{at}}\right) \quad (2)$$

Where γ_{hkl}^{int}, θ, A_{at}, E_{ads} is DFT-calculated interfacial tension, the equilibrium coverage of H_2O,

the surface area per surface atom and the adsorption energy of H_2O.

$$E_{ads} = E\left(\mathrm{H_2O/slab}\right) - E\left(\mathrm{slab}\right) - E\left(\mathrm{H_2O_{(g)}}\right) \tag{3}$$

Where $E(H_2O/slab)$, $E(slab)$, and $E(H_2O_{(g)})$ denote DFT-calculated total energy of slab with adsorbed H_2O, clean slab and gas-phase H_2O, respectively. Here, slab denotes a specific Miller low-index facet.

The Langmuir adsorption isotherm is applied to obtain the equilibrium coverage (θ) in the adsorption/desorption process of the water vapor on three Miller low-index facets:

$$\theta = \frac{\theta_{\mathrm{ML}} PK}{\left(1 + PK\right)} \tag{4}$$

Where θ_{ML} is the monolayer coverage of H_2O[58-60] on (110), (100) and (111) facets corresponding to θ_{ML} = 0.67, 1.0 and 0.67, respectively, derived from DFT-calculated results (Figure S1). P and K represent the pressure and equilibrium constant (Langmuir isotherm constant), respectively.

$$K = \exp\left(-\frac{\Delta G}{k_{\mathrm{B}} T}\right) = \exp\left(-\frac{E_{\mathrm{ads}} - T\left(S_{\mathrm{ads}} - S_{\mathrm{gas}}\right)}{k_{\mathrm{B}} T}\right) \tag{5}$$

Where k_B is the Boltzmann constant, S_{ads} and S_{gas} are the entropy of adsorbed and gas-phase H_2O molecule retrieved from the NIST Chemistry WebBook.[61] Here, S_{ads} is adopted as the entropy of ice considering the interfacial water monolayer on metal surface normally forms an ice-like structure.[59-60] The water vapor at given temperature of 300 K - 900 K and pressure of 1 Pa - 250 Pa was considered in this study.

The Rh and Ir nanoparticles were modeled using the multiscale operando simulation package (MOSP).[50] The well-defined particle structures of three sizes were constructed with diameter (d) ≈ 3.5 nm, 5.5 nm and 9.5 nm (measured as the longest distance between two vertices of truncated octahedron) containing around 1571, 7530 and 31121 atoms, respectively, for complete closure of a NP without creating defects on each facet. The distinctive structures of NPs can be quantified by *average* atomic coordination number ($\overline{CN}$) of surface atoms, which serve as an important morphology parameter:

$$\overline{CN} = \sum_{\mathrm{i}=1}^{\mathrm{surf}} (CN_{\mathrm{i}}) / N_{\mathrm{surf}} \tag{6}$$

Where CN_i is the coordination number of the ith surface atom and N_{surf} is the total number of

surface atoms of the NP. Note here that the same-sized NPs with different $\overline{CN}$ may contain slightly different total number of atoms (±5% in variation), which are expected not to severely influence calculated results and thereafter the final conclusion.

As is known, the high Miller-index facets have higher surface energy than the low Miller-index facets resulting in their negligible contributions to metal NP's morphology. We thus choose the three low-index facets, i.e., (111), (100) and (110) terraces (with CN_i = 9, 8 and 7, respectively), which have been observed to be most important for defining the shape of fcc-metal NPs and have been commonly employed for exploring their morphology evolution,[33, 50-51] along with edge and corner sites with CN_i = 6 and 5, and atoms in bulk with CN_i > 9. The surface atomic concentration (η) of specific coordination number, equivalent to surface sites concentrations, can be used to characterize various adsorption sites and to account for the intrinsic morphological heterogeneity of NPs, defined as:

$$\eta_i = \frac{N_i}{N_{surf}} * 100\% \tag{7}$$

The weighted work function ($\overline{\Phi}$) of NP is introduced to provide an additional measure of structural evolution of NPs, defined as:

$$\overline{\Phi} = \frac{\sum_{\{hkl\}} \Phi_{hkl} A_{hkl}}{\sum A_{hkl}} \tag{8}$$

Where A_{hkl} is the area of all facets of the {hkl} family in the Wulff construction. Φ_{hkl} is the work function for a specific facet.

The total surface tension ($\overline{\gamma_{hkl}}$) of NP is introduced as a measure of surface relative stability of NPs, defined as:

$$\overline{\gamma_{hkl}} = \frac{\sum_{\{hkl\}} \gamma_{hkl} A_{hkl}}{\sum A_{hkl}} \tag{9}$$

Where γ_{hkl} is the surface tension for a specific facet existing in the Wulff construction.

The total water-metal interfacial tension ($\overline{\gamma_{hkl}^{int}}$) of NP is introduced as a measure of the relative stability of NPs in water vapor envirvorment, defined as:

$$\overline{\gamma_{hkl}^{int}} = \frac{\sum_{\{hkl\}} \gamma_{hkl}^{int} A_{hkl}}{\sum A_{hkl}} \tag{10}$$

where γ_{hkl}^{int} is the interfacial tension for a specific facet existing in the Wulff construction. Note

here that γ_{hkl}^{int} at steps/edges due to water adsorption is not considered based on DFT-calculated results showing that the binding strength of H_2O at edges sites (using (221) surface as the model)[62] are smaller than those on (110) facets of Rh and Ir NPs (Table S1).

2.2. DFT Calculations.

The spin-polarized periodic DFT calculations were performed using Vienna ab-initio simulation package (VASP)[63] with the projector augmented-wave method (PAW).[64] A plane-wave cutoff energy of 450 eV and the convergence criteria of 10^{-5} eV in electronic relaxation and 0.01 eV/Å in force with conjugate-gradient algorithm were adopted. For surface tension, Perdew-Burke-Ernzerhof (PBE) functional[51] within generalized gradient approximation (GGA)[65] was employed. The Brillouin zone of the periodic two-dimensional (2-D) (1×1) slab was sampled by a (16×16×1) Monkhorst-Pack grid of K-points.[66] Slabs containing 13 atomic layers were used to calculate surface energy with middle 7 layers fixed at bulk position (Rh: 3.804 Å, Ir: 3.839 Å) and up-and-bottom 3 layers relaxed following the methodology suggested by Fiorentini and Methfessel.[67] For adsorption energy of H_2O, an accurate exchange functional optPBE[68] for the vdW correlation functional was employed for accounting for van der Waals (vdW) interaction of H_2O with metal surfaces. The Γ-centered 3×3×1 K-points grids was set for Brillouin zone of periodic 2-D (4×4) slabs, which were separated with a 15 Å vacuum space along the Z axis. Each slab contains 6 layers with the bottom 2 layers fixed in geometry optimization. Our DFT-calculated results of surface energy (γ_{hkl}) and adsorption energy (E_{ads}) (listed in Table S1) agree well with those reported in previous studies.

2.3. Molecular Dynamics. (MD)

Thermal annealing of metal NPs in vacuum was simulated using a large-scale atomic/molecular massively parallel simulator (LAMMPS),[69] which has been widely employed for studying structural phase transitions of metals.[54] The embedded atom method (EAM) many-body potentials of Rh and Ir proposed by Sheng et al[70] (Supporting Information) were used to determine the interaction energy of Rh - Rh and Ir - Ir atoms for all MD annealing simulations. A Nosé-Hoover thermostat and barostat were employed to control temperature and pressure, respectively. The velocity Verlet scheme was used for solving the equations of motion with the constant time step of 1 fs with a damping parameter of 0.1 ps controlling the temperature throughout.[71] The simulations of NPs were performed using NVT ensemble with incremental heating (300 - 900 K) at a ramping rate of 200 K/ns and running for 5 ns

at each temperature (T = 300 K, 500 K, 700 K and 900 K). Similarly, the simulations of bulk Rh and Ir were performed using a 10×10×10 supercell (containing 4000 atoms) and NPT ensemble for their potential binding energies at each temperature and 1 bar. The energetic values are averaged over the last 1 ns of simulation. Prior to MD run, the NP structures were first optimized with the convergence threshold of 10^{-7} eV for energy and 10^{-9} eV/Å for force. In total, 30 well-defined particle structures of varied $\overline{CN}$ were studied for each size ($d \approx$ 3.5 nm, 5.5 nm and 9.5 nm). The snapshots of NPs were visualized using OVITO package.[72]

The structural transformation inertness (Δ) of NPs is defined as:[73]

$$\Delta = (E_{\mathrm{NP}} - NE_{\mathrm{bulk}})/N^{2/3} \tag{11}$$

Where Δ is the excess energy roughly per surface atom of NP as a result of transformation of bulk metal at T K into the corresponding NPs at T K. E_{NP} and E_{bulk} are MD-calculated potential binding energy of NP consisting of N number of atoms and its bulk counterpart (per atom) at T K, respectively. Less positive values represent NP structure resembling more closely its bulk counterpart and thus being higher of the structural transformation inertness.

The percentage of surface over total atoms of NP can be calculated as:

$$S = N_{\mathrm{surf}} / N * 100\% \tag{12}$$

Where N_{surf} and N are the number of surface atoms and total number of atoms in NP, respectively.

3. RESULTS AND DISCUSSION

3.1. Shape/Size-Dependent Structural Reconstruction of NPs under Annealing Conditions.

The shape/size of metal NPs has important influence on their exceptional functionality and reactivity. Metal nanoparticles of up to 5-nm size commonly exhibit remarkable particle-size effect on enhancing catalytic performance.[5, 19, 21, 74] It was reported that the tendency of Rh NPs to become oxidized is also size-dependent, i.e., remaining metallic if larger than 4-nm size while being oxidized if smaller than 2.5-nm size.[21, 62, 74] Hence, we chose 5.5 nm-size Rh and Ir nanoparticles (around 7500 atoms) with sufficient number of isomers for their shape-dependent structural reconstruction with increasing temperature of 300 K - 900 K, whose range covers ambient to moderate-to-high temperatures (550 K - 900 K) relevant to various catalytic applications (e.g., DEFC, OER, SRM, SRE, TWC and HDO).[9-18] The initial particle structures were built based on Wulff-Gibbs theorem that dictates a single crystal of an fcc metal (e.g., Rh and Ir) should assume a truncated octahedron as its

equilibrium shape in vacuum.

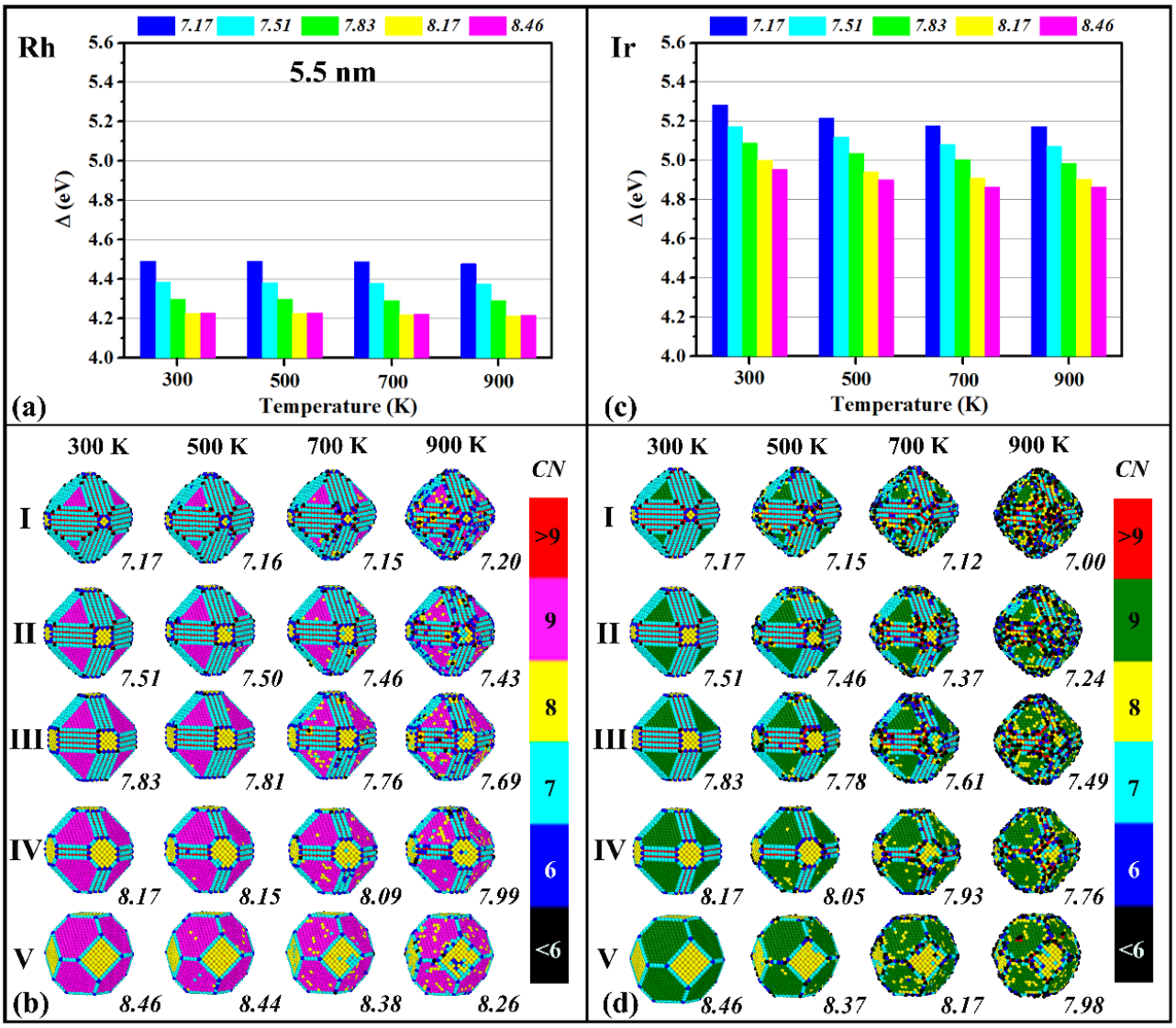

Figure 1. Thermal stability and structural reconstruction of metal nanoparticles (d = 5.5 nm) with increased temperature. Rh: (a) structural transformation inertness (Δ), (b) snapshots; Ir: (c) structural transformation inertness (Δ), (d) snapshots. For clarity, atoms with corresponding *CN* are depicted in the same colors. Italic numbers: $\overline{CN}$.

Table S2 lists the potential binding energy (BE) of bulk metals under annealing temperature of 300 K-900 K, showing that bulk Ir is thermodynamically more stable than bulk Rh at given annealing temperature, consistent with the higher melting point (MP) of bulk Ir than Rh, i.e., MP(Ir) = 2739 K vs. MP(Rh) = 2237K. However, metal NPs experience initial structural reconstruction inevitably from the surface rather than in the bulk underneath due to their intrinsic surface energy. As shown in Figure 1, the distinctive morphology of particle structure (**I** - **V**) at T = 300K was generated being as

edge/corner-truncated octahedral structure corresponding to $\overline{CN}$ = 7.2, 7.5, 7.8, 8.2, or as truncated octahedral structure corresponding to $\overline{CN}$ = 8.5. Six types of surface atoms are observed from the equilibrium shape of NPs: (i) bulk atoms with $CN > 9$; (ii) (111)-terrace atoms with $CN = 9$; (iii) (100)-terrace atoms with $CN = 8$; (iv) (110)-terrace atoms with $CN = 7$; (v) edge-site atoms between (100) and (110) terrace with $CN = 6$; (vi) corner-site atoms with $CN < 6$. Besides **V** structure which is a truncated octahedron that is thermodynamically most favorable, **I** - **IV** structures can be regarded as the representative NPs synthesized under certain kinetically-controlled conditions.

With elevated annealing temperature, both Rh and Ir NPs like their bulk counterparts become thermally less stable with dynamic characteristics (Figure S2-S3 and Table S2). As can be seen from the ordering of Δ values, the structural transformation inertness and thermal stability of 5-nm NPs follows the order of **I** < **II** < **III** < **IV** < **V** (**IV** ≈ **V** for Rh) (with increasing $\overline{CN}$) at any specific annealing temperature, causing a more facile structural transformation of a NP with a lower $\overline{CN}$. The same trend can also be found from both 3.5-nm and 9.5-nm NPs (Figure S4-S5), suggesting NP structure as a whole become thermally more stable with the increased $\overline{CN}$ till up to the scalable regime reaching the ultimate upper limit of bulk metals. Using NPs of 300 K as references, the initial NP structures with lower $\overline{CN}$ (e.g., 7.17 of **I**) are more sensitive to annealing temperature than those with higher $\overline{CN}$ (e.g., 8.46 of **V**) resulting in severe structural transition especially for smaller-size NPs (Figure S4). This can be explained mainly by that (110) facets together with edge/corner sites dominating a NP surface of lower $\overline{CN}$ could have much higher surface tension than (111) facets dominating a NP of higher $\overline{CN}$ (Table S1). Both Rh and Ir NPs have undergone gradually noticeable structural transformation on the surface with the sizeable decreases of $\overline{CN}$ especially for Ir NPs. Remarkably, such a structural transformation occurs more often at the boundary than at terrace sites on the surface, visualized by the snapshots of NPs. Additionally, the effect of annealing on weakening the thermal stability of NPs are nearly the same in magnitude for **I** - **V** structures regardless of their differed $\overline{CN}$, suggesting the potential binding energy of bulk atoms of NPs contributes most to maintaining the thermal stability. In comparison, the structural transformations are more pronounced for Ir NPs than Rh NPs due to their higher surface tension (Table S1). Our MD results agree well with the experimental observations that migration and coalescence of Ir particles take place above 700 K lower than those of Rh particles up to 900 K.[75-76] Furthermore, it is worthy to note that our simulated XRD spectra suggest there exist no phase transformation up to 900 K even for 3.5 nm Rh and Ir NPs,

which resemble their bulk phase (Figure S6).

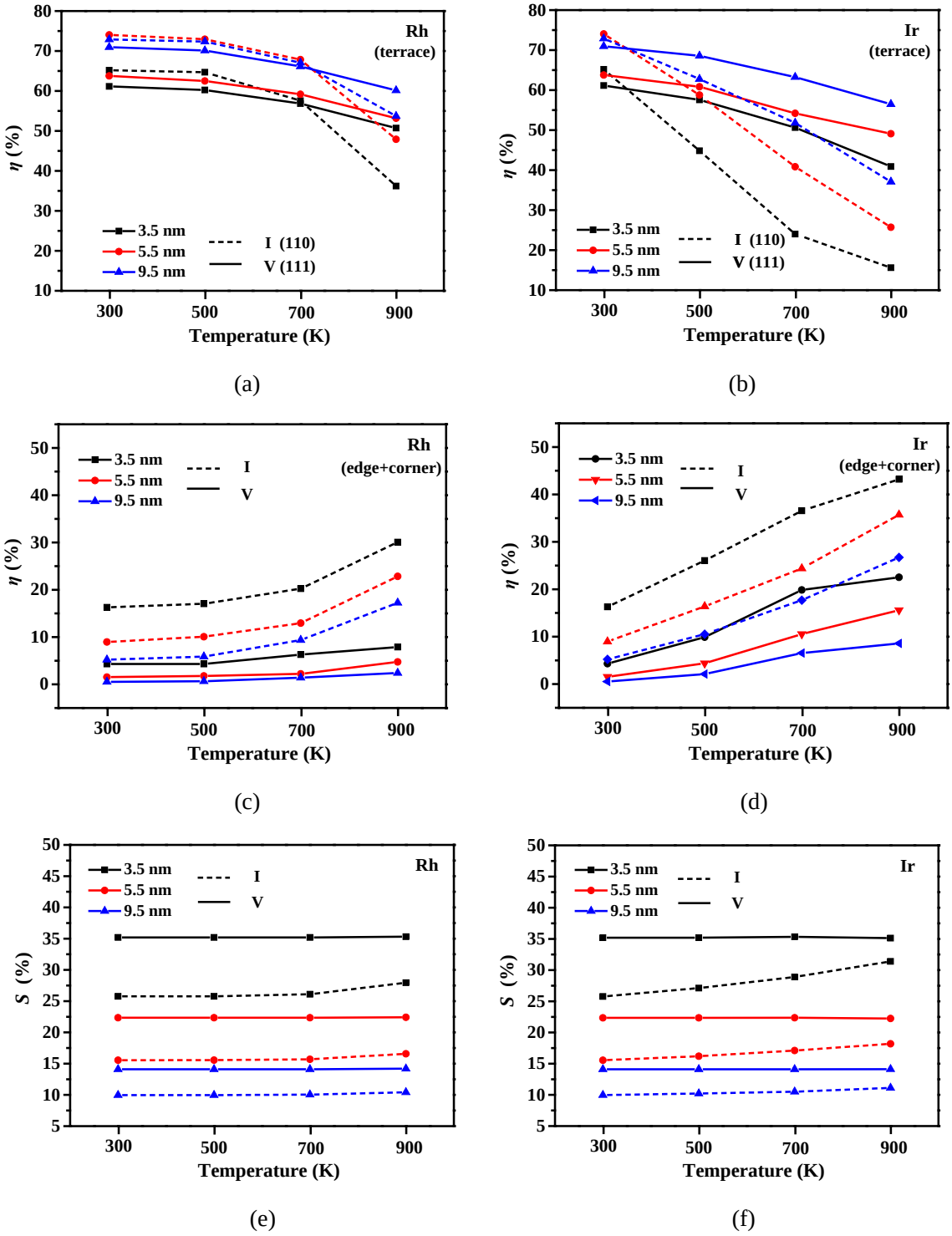

Figure 2. (a)-(d)Surface atomic concentration (η) of terrace and edge/corner sites as a dependence of annealing temperature; (e)-(f) Percentage of surface atoms (S) as a dependence of annealing temperature.

Using **I** and **V** as the representatives for NPs synthesized by kinetically- and thermodynamically-controlled means, respectively, we further examine structural changes on the surfaces. Figure 2a-2b

show that surface atomic concentration (η) of the most dominant terrace sites, i.e., (110) for **I** and (111) for **V**, are greatly lowered as annealing temperature increases from 300 K to 900 K particularly for (110) terrace. The loss of terraces sites is more severe on Ir NP than Rh NP, and on smaller-size NP than larger-size NP, accompanied by the gain of edge/corner sites (Figure 2c-2d), which was also observed by previous study on annealing process of fcc-metal Pt NPs with similar sizes.[54] For example, terrace sites of 3.5 nm-, 5.5 nm-, and 9.5 nm-NPs have η(%)/facet = 65.2/(110), 74.0/(110), 72.9/(110) for **I**, and 61.2/(111), 63.8/(111), 71.0/(111) for **V** at 300 K, which are reduced to 36.1/(110), 48.0/(110), 53.7/(110), and 50.7/(111), 53.2/(111), 60.1/(111) for Rh NP, but are reduced to 15.6/(110), 25.7/(110), 37.1/(110), and 40.9/(111), 49.1/(111), 56.5/(111) for Ir NP at T = 900 K; meanwhile, edge/corner sites of η(%)/structure = 16.3, 9.0, 5.2 for **I**, and 4.3, 1.5, 0.5 for **V** at T = 300 K are increased to η(%)/structure = 30.1, 22.8 and 17.3 for **I**, 7.9, 4.8 and 2.4 for **V** (Rh NP) but to η(%)/structure = 43.2, 35.7 and 26.7 for **I**, 22.5, 15.6 and 8.6 for **V** (Ir NP) at T = 900 K. Moreover, the ratio of surface to total atoms of NP is decreased with the increased particle size and in comparison, **I** structure with a lower $\overline{CN}$ has the smaller percentage of surface atoms than **V** structure with a higher $\overline{CN}$. With enhanced temperature, there exists certain degree of bulk-to-surface atom transfer particularly for **I** structure of small-size (3.5-nm) NPs at high annealing temperature of 900 K (Figure 2e-2f), e.g., S (%) = 25.8 at 300 K, increased to 27.9 for Rh NP and 31.4 for Ir NP at 900 K. Our findings provide valuable information on how the surface sites of a multifaceted metal NP are varied with elevated temperature, which is of particular importance to many catalytic reactions, e.g., edge/corner sites for steam methane reforming[13] and CO oxidation,[21] terrace sites for CO hydrogenation.[19]

3.2. Shape Evolution of NPs under Water Vapor Conditions.

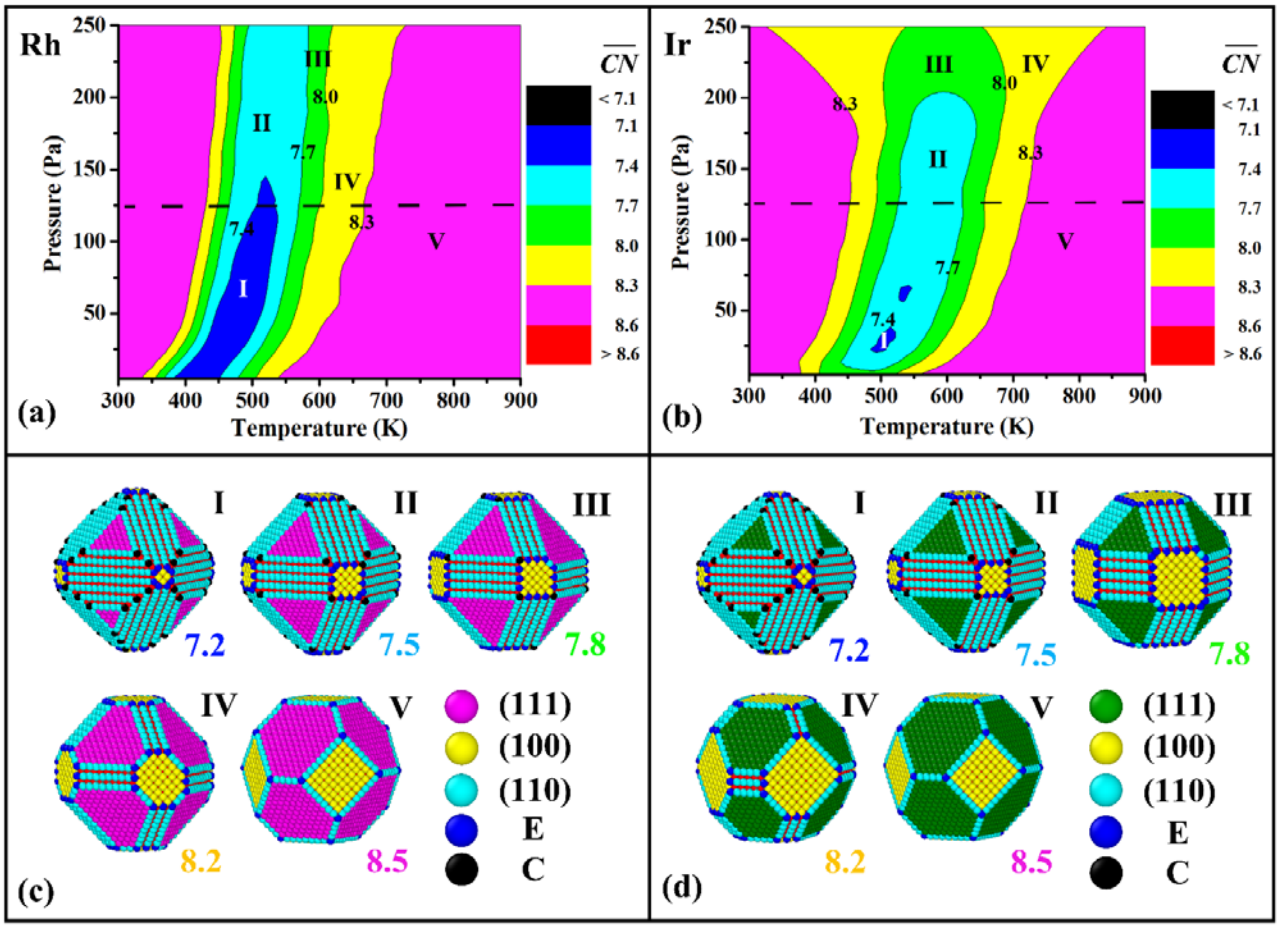

Figure 3. Structural isosurface ($\overline{CN}$) of 5.5-nm NPs of (a) Rh and (b) Ir as functions of temperature and pressure of water vapor (varying by 5 K and 5 Pa for each data point). Representative NP structures (**I - V)** of (c) Rh and (d) Ir corresponding to five typical regions (with the matched color). Black dashed line: at 125 Pa. E: edge sites; C: corner sites.

Water atmosphere is ubiquitous in many technically-relevant applications such as heterogeneous and electrochemical catalysis being as reactant, reaction intermediate and product. We examined the effect of water vapor on shape evolution of Rh and Ir NPs at given temperature of 300 K - 900 K (Section 3.1) and pressure of 1 Pa - 250 Pa,[33-34] which has been observed to exert significant impact on shape evolution of fcc-metal NPs sensitive to even a small variation. Indeed, as shown in Figure 3, the interplay of temperature and pressure of water vapor (P, T) greatly induce surface structural reconstruction of 5.5-nm Rh and Ir NPs leading to the variation of $\overline{CN}$ (= 7.2, 7.5, 7.8, 8.2, 8.5) and accordingly, the remarkable shape evolution. For example, Figure 3a and 3c and Table S3 show that with increased temperature at P = 125 Pa, the equilibrium shape of Rh truncated octahedron (**V**, $\overline{CN}$ = 8.5) built up with (111) and (100) facets at 300 K evolves to edge/corner-truncated octahedra (**I - IV**,

$\overline{CN}$ = 7.2 - 8.2) with (110) facets being emerged from 425 K to 675 K. Interestingly, beyond 675 K, NPs are capable of further evolving back to truncated octahedron (**V**, $\overline{CN}$ = 8.5). Here, the blue region (**I** structure) is the lowest ($\overline{CN}$ = 7.2) in structural isosurface and in between (**II** - **IV**) can be regarded as the transition zone between **I** and **V** structures. However, beyond 140 Pa, Rh NPs can directly evolve back to truncated octahedron without passing through **I** structure. Similar shape evolution can also be found from Ir NPs except that the blue region (**I** structure) is not prerequisite for transition between the two pink regions (**V**). Furthermore, 3.5-nm and 9.5-nm NPs of Rh and Ir exhibit similar shape evolution except the slight variation of $\overline{CN}$ due to size effect (Figure S7-S8). Overall, an increase/decrease in the ratio of (110)/(111) facets contribute most to the decreasing/increasing of $\overline{CN}$ under the influence of water vapor at pressures of a few mbars leading to a reversible shape transformation of Rh and Ir NPs, which phenomenon is not uncommon for experimentally observed fcc-metal NPs in various gaseous environments (*P*, *T*) including water.[3, 33, 77] The structural isosurface pattern seems to indicate that the shape evolution of Rh and Ir NPs is more sensitive to temperature than pressure of water vapor leaving the surface of NPs in a metastable state, consistent with the previous findings from other fcc metals, e.g., Cu.[51] Moreover, it should be noted that the NPs of the same $\overline{CN}$ can have isomeric structures (e.g., $\overline{CN}$ = 8.2 for **IV** of Rh and Ir NPs) and more isomers are likely to emerge as particle size increases.

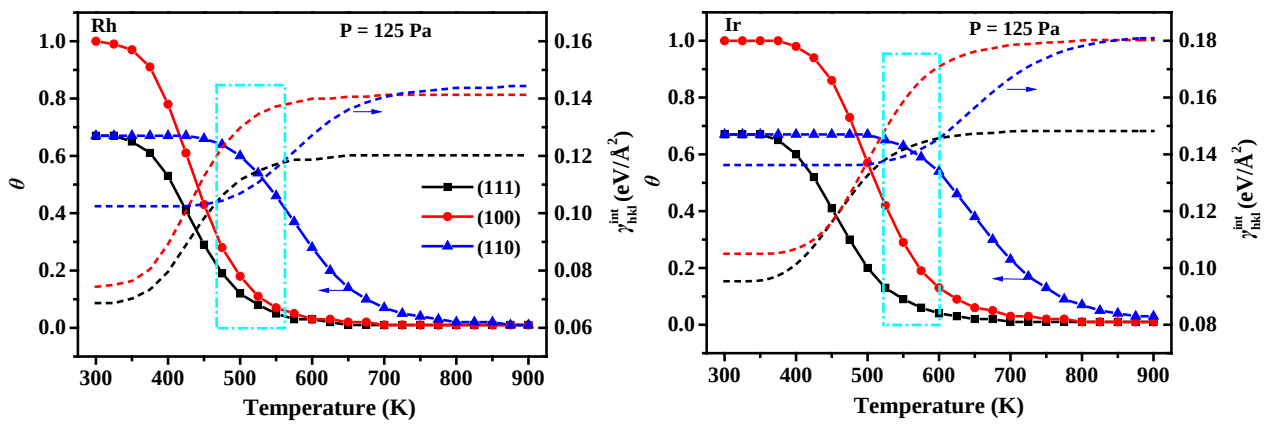

(a) (b)

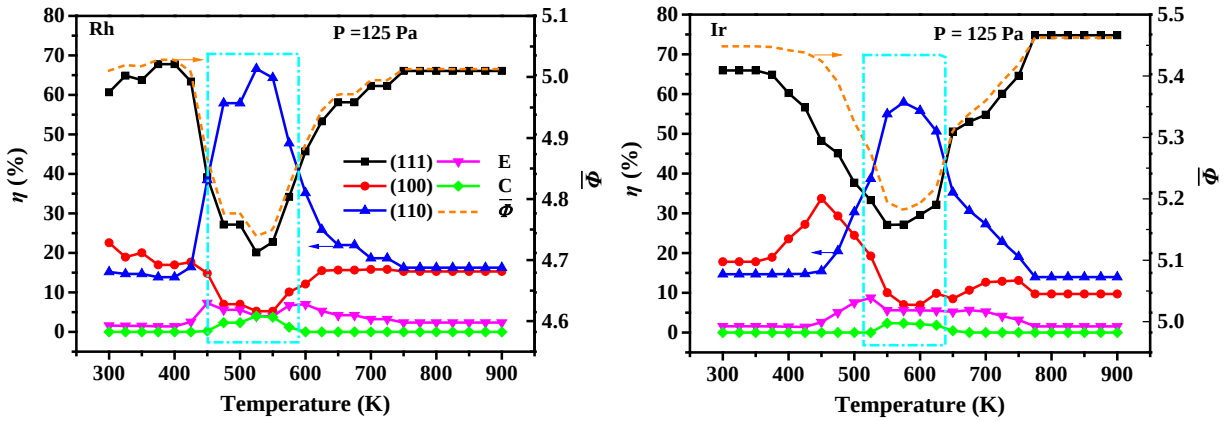

(c) (d)

Figure 4. H_2O coverage (θ) and interfacial tension (γ_{hkl}^{int}) of different facets as a function of temperature at 125 Pa (a) Rh and (b) Ir. Atomic concentration (η) of different facets, edge (E)/corner (C) and weighted work function ($\bar{\Phi}$) of NPs as a function of temperature at 125 Pa (c) Rh and (d) Ir. Dashed-dotted rectangle: transition zone. See also Figure S9 for three-dimensional contour.

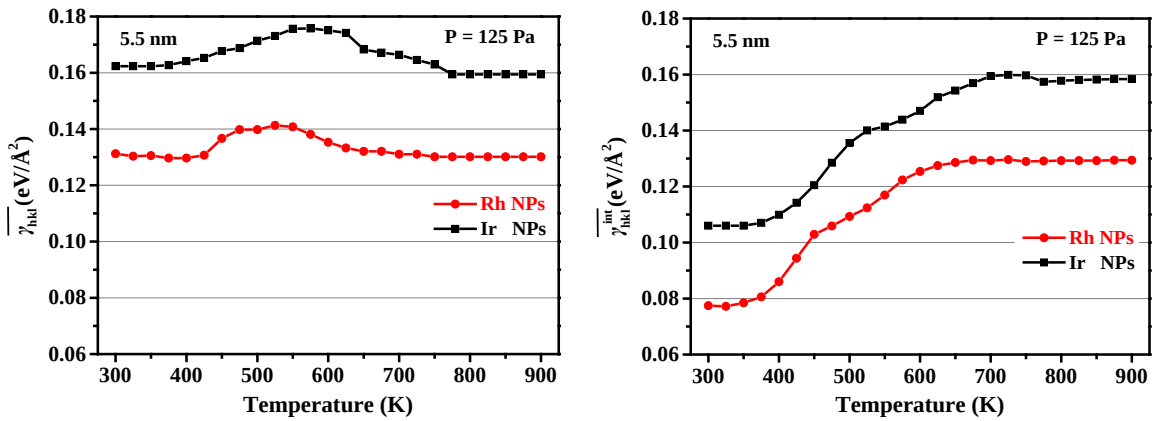

(a) (b)

Figure 5. Variation of total surface tension ($\overline{\gamma_{hkl}}$) and total interfacial surface tension ($\overline{\gamma_{hkl}^{int}}$) of NPs as a function of temperature.

We further explored the underlying of such a shape evolution and the arisen effect. As shown in Figure 4a-4b, the variations of H_2O coverage (θ) and interfacial tension (γ_{hkl}^{int}) of different facets form the opposite (or mirrored) trend (solid vs dashed lines) as a dependence of elevated temperature of 300 K - 900 K, in which γ_{hkl}^{int} is the lowest with nearly the full coverage of H_2O at low-temperature end with $\gamma_{hkl}^{int}(110) > \gamma_{hkl}^{int}(100) > \gamma_{hkl}^{int}(111)$, and increases as H_2O coverage decreases till its complete desorption at high-temperature end with $\gamma_{hkl}(110) > \gamma_{hkl}(100) > \gamma_{hkl}(111)$, i.e., equivalent to pristine NPs. This explains the existence of the two same pink regions at the two ends of temperature forming

the equilibrium shape of truncated octahedron (**V**) dictated by Wulff construction. Specifically, there exists two crossovers between interfacial tension of (111) and (110) facets (highlighted in rectangle) corresponding to the temperature range of 475 K - 575 K, which falls in the transition zone (Figure 3a -3b), suggesting the competition between the interfacial tension of (111) and (110) facets plays a major driving force for shape evolution to minimize the total surface tension of Rh and Ir NPs (Figure 5a). However, the total interfacial tension of NPs is raised with elevated temperature up to the upper limit of total surface energy, resulting in NPs having the same $\overline{CN}$ (e.g., 8.5) is more stable with H_2O adsorbed at low temperature than those with H_2O desorbed at high temperature (Figure 5b). Note that total interfacial tension originates from the interplay of surface tension, adsorption energy and coverage of adsorbate. Hence, the potential energy surface of adsorbate-NP system in a variable gaseous environment (P, T) can be accurately described by the variation of total interfacial tension of NPs.

Moreover, the variations of atomic concentrations (η) of (111) and (110) facets follow the opposite (or mirrored) trend where the values of η are changed substantially with atoms of (111) facet being reconstructed into atoms of (110) facet in the same temperature range (rectangle in Figure 4c-4d) specifically for Rh at 525 K and Ir at 600 K, where H_2O coverage of $\theta_{110} >> \theta_{111}$ leads to surface atomic concentrations of $\eta_{110} >> \eta_{111}$. Interestingly, the weighted work function ($\overline{\Phi}$) of Rh and Ir NPs can be tuned such that $\overline{\Phi}$ varies nearly the same/opposite trend of η_{111}/η_{110}, which has implication of potential applications in environmental, chemical and biological sensing of water.[78-79] Additionally, both Rh and Ir NPs could be more resistant to water corrosion than Pd and Pt NPs[51] as a higher temperature is needed to reach the same minimum $\overline{CN}$ (= 7.2). In comparison, Ir NPs are better than Rh NPs in resisting water corrosion.

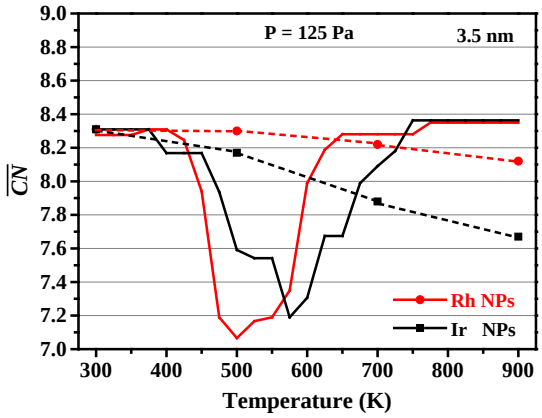

(a)

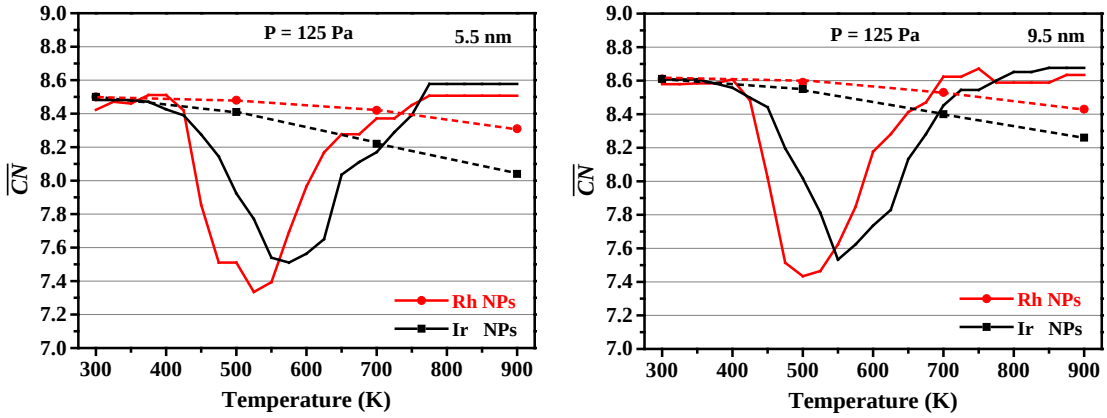

(b) (c)

Figure 6. Variation of $\overline{CN}$ of different size: (a) 3.5-nm; (b) 5.5-nm; (c) 9.5-nm of truncated octahedral (**V**) NPs as a function of temperature in vacuum and in water vapor conditions. Dash lines: in vacuum. Solid lines: in water vapor.

Overall, it is apparent that the structural reconstruction of Rh and Ir NPs is dynamic under either annealing or water vapor condition. However, there is great discrepancy in their structural evolution process (Figure 6), that is, it is an irreversible/reversible process under the former/latter condition. With increased temperature of 300 K - 900 K, $\overline{CN}$ of either Rh or Ir NP becomes gradually lowered by annealing, presumably reaching minimal $\overline{CN}$ at surface melting point (lower than that of bulk counterpart). As can be seen, the $\overline{CN}$ is lowered more rapidly with the increasing of temperature for smaller-sized NPs than that for larger-sized NPs, i.e., $\overline{CN}$/T: 3.5-nm > 5.5-nm > 9.5-nm, and comparatively, Ir > Rh, implicating that smaller-sized NPs could have lower surface melting point than the larger-sized ones. By contract, the variation of $\overline{CN}$ of either Rh or Ir NP with temperature in water vapor envirvorment (with constant pressure) forms a reversed-volcano shape plot, indicating that water vapor can drive the shape evolution process in a reversible fashion.

4. Conclusion

By means of Wulff construction combined with DFT and MD calculations, we have systematically investigated the shape/size-dependent structural reconstruction of truncated octahedron-based Rh and Ir NPs under annealing and water vapor conditions. The major conclusions are as follows: (1) The average atomic coordination number ($\overline{CN}$) of surface atoms is reconfirmed as a key morphology parameter for metal NPs and the total adsorbate-metal interfacial tension can serve as a key stability parameter for metal NPs in a variable gaseous environment (P, T). (2) The NPs having lower $\overline{CN}$ are more sensitive to annealing temperature than those with higher $\overline{CN}$, resulting in more

severe structural transition especially for smaller-sized NPs and Ir NPs due to their lowered structural transformation inertness and thermal stability. (3) Under water vapor conditions, the competition between the interfacial tension of (111) and (110) facets is a major driving force for shape evolution by minimizing the total surface tension of Rh and Ir NPs. The potential energy surface of adsorbate-NP system can be accurately described by the variation of total interfacial tension of metal NPs. (4) It is revealed that annealing in vacuum/water vapor condition proceeds in an irreversible/reversible fashion on Rh and Ir NPs, indicating the significance of *in situ* probing the morphology of metal NPs to relevant applications.

ASSOCIATED CONTENT

Supporting Information

The Supporting Information is available free of charge on the ACS Publications website at DOI: 10.1021/acs.jpcc. xxxxxxx.

DFT-calculated data and optimized structures; MD-calculated potential energy profiles, thermal stability and structural reconstruction of 3.5-nm and 9.5-nm NPs; Structural isosurface ($\overline{CN}$) of 3.5-nm and 9.5-nm NPs; Three-dimensional contour of H_2O coverage and interfacial tension on different facets of 5.5 nm NPs as a function of temperature and pressure of water vapor.

The EAM potentials of Rh and Ir proposed by H.W.Sheng.

AUTHOR INFORMATION

Corresponding Author

*E-mail: weian@sues.edu.cn.

Notes

The authors declare no competing financial interest.

ACKNOWLEDGMENTS

This work was supported by the National Natural Science Foundation of China (21673137), the Science and Technology Commission of Shanghai Municipality (16ZR1413900). The DFT calculations were performed by using resources of the Center for Functional Nanomaterials, which is a U.S. DOE Office of Science Facility, and the Scientific Data and Computing Center, a component of the Computational Science Initiative, at Brookhaven National Laboratory under Contract No. DE-SC0012704. The authors are grateful to Drs. Yi Gao and Beien Zhu at Shanghai Advanced Research

Institute, Chinese Academy of Sciences for providing MOSP code and valuable discussions.

REFERENCES

1. Zhou, Z. Y.; Tian, N.; Li, J. T.; Broadwell, I.; Sun, S. G., Nanomaterials of High Surface Energy with Exceptional Properties in Catalysis and Energy Storage. *Chem. Soc. Rev*. **2011**, *40*, 4167-4185.

2. Vines, F.; Gomes, J. R.; Illas, F., Understanding the Reactivity of Metallic Nanoparticles: Beyond the Extended Surface Model for Catalysis. *Chem. Soc. Rev.* **2014**, *43*, 4922-4939.

3. Zhu, B.; Meng, J.; Yuan, W.; Zhang, X.; Yang, H.; Wang, Y.; Gao, Y., Reshaping of Metal Nanoparticles in Reaction Conditions. *Angew. Chem. Int. Ed.* **2019**.

4. Younan, X.; Yujie, X.; Byungkwon, L.; Skrabalak, S. E., Shape-Controlled Synthesis of Metal Nanocrystals: Simple Chemistry Meets Complex Physics? *Angew. Chem. Int. Ed.* **2013**, *38*, 335-344.

5. Yuan, Y.; Yan, N.; Dyson, P. J., Advances in the Rational Design of Rhodium Nanoparticle Catalysts: Control Via Manipulation of the Nanoparticle Core and Stabilizer. *ACS Catal.* **2012**, *2*, 1057-1069.

6. Cao, S.; Tao, F. F.; Tang, Y.; Li, Y.; Yu, J., Size-and Shape-Dependent Catalytic Performances of Oxidation and Reduction Reactions on Nanocatalysts. *Chem. Soc. Rev.* **2016**, *45*, 4747-4765.

7. Mostafa, S.; Behafarid, F.; Croy, J. R.; Ono, L. K.; Li, L.; Yang, J. C.; Frenkel, A. I.; Cuenya, B. R., Shape-Dependent Catalytic Properties of Pt Nanoparticles. *J. Am. Chem. Soc.* **2010**, *132*, 15714-15719.

8. Burda, C.; Chen, X.; Narayanan, R.; El-Sayed, M. A., Chemistry and Properties of Nanocrystals of Different Shapes. *Chem. Rev.* **2005**, *105*, 1025-1102.

9. Suo, Y.; Hsing, I. M., Highly Active Rhodium/Carbon Nanocatalysts for Ethanol Oxidation in Alkaline Medium. *J. Power Sources*. **2011**, *196*, 7945-7950.

10. De Tacconi, N. R.; Lezna, R. O.; Beden, B.; Hahn, F.; Lamy, C., In-Situ FTIR Study of the Electrocatalytic Oxidation of Ethanol at Iridium and Rhodium Electrodes. *J. Electroanal. Chem.* **1994**, *379*, 329-337.

11. Reier, T.; Oezaslan, M.; Strasser, P., Electrocatalytic Oxygen Evolution Reaction (OER) on Ru, Ir, and Pt Catalysts: A Comparative Study of Nanoparticles and Bulk Materials. *ACS Catal.* **2012**, *2*, 1765-1772.

12. Özer, E.; Spöri, C.; Reier, T.; Strasser, P., Iridium (111), Iridium (110), and Ruthenium (0001) Single Crystals as Model Catalysts for the Oxygen Evolution Reaction: Insights into the Electrochemical Oxide Formation and Electrocatalytic Activity. *ChemCatChem*. **2017**, *9*, 597-603.

13. Ligthart, D. A. J. M.; Van Santen, R. A.; Hensen, E. J. M., Influence of Particle Size on the Activity and Stability in Steam Methane Reforming of Supported Rh Nanoparticles. *J. Catal.* **2011**, *280*, 206-220.

14. Spivey, J. J.; Egbebi, A., Heterogeneous Catalytic Synthesis of Ethanol from Biomass-Derived Syngas. *Chem. Soc. Rev.* **2007**, *36*, 1514-1528.

15. An, W.; Men, Y.; Wang, J.; Liu, P., Interfacial and Alloying Effects on Activation of Ethanol from First-Principles. *J. Phys. Chem. C*. **2017**, *121*, 5603-5611.

16. Srinivasan, A.; Depcik, C., Review of Chemical Reactions in the NO Reduction by CO on Rhodium/Alumina Catalysts. *Chem. Rev.* **2010**, *52*, 462-493.

17. Zhou, L.; Lawal, A., Hydrodeoxygenation of Microalgae Oil to Green Diesel over Pt, Rh and Presulfided NiMo Catalysts. *Catal. Sci. Technol.* **2016**, *6*, 1442-1454.

18. Nhung N. Duong; Darius Aruho; Bin Wang; Resasco, D. E., Hydrodeoxygenation of Anisole over Different Rh Surfaces. *Chin. J. Catal.* **2019**.

19. Ojeda, M.; Rojas, S.; Boutonnet, M.; Pérez-Alonso, F. J.; García-García, F. J.; Fierro, J. L. G., Synthesis of Rh Nano-Particles by the Microemulsion Technology: Particle Size Effect on the CO+H_2 Reaction. *Appl. Catal., A*. **2010**, *274*, 33-41.

20. Nguyen, L.; Liu, L.; Assefa, S.; Wolverton, C.; Schneider, W. F.; Tao, F. F., Atomic-Scale Structural Evolution of Rh (110)

During Catalysis. *ACS Catal.* **2016**, *7*, 664-674.

21. Grass, M. E.; Yawen, Z.; Butcher, D. R.; Park, J. Y.; Yimin, L.; Hendrik, B.; Bratlie, K. M.; Tianfu, Z.; Somorjai, G. A., A Reactive Oxide Overlayer on Rhodium Nanoparticles During CO Oxidation and Its Size Dependence Studied by in Situ Ambient-Pressure X-Ray Photoelectron Spectroscopy. *Angew. Chem. Int. Ed.* **2010**, *47*, 8893-8896.

22. Wang, H.; Shan, Z.; Gilroy, K. D.; Cai, Z.; Xia, Y., Icosahedral Nanocrystals of Noble Metals: Synthesis and Applications. *Nano Today*. **2017**, *15*, 121-144.

23. Wu, B.; Zheng, N., Surface and Interface Control of Noble Metal Nanocrystals for Catalytic and Electrocatalytic Applications. *Nano Today*. **2013**, *8*, 168-197.

24. Biacchi, A. J.; Schaak, R. E., The Solvent Matters: Kinetic Versus Thermodynamic Shape Control in the Polyol Synthesis of Rhodium Nanoparticles. *Acs Nano*. **2011**, *5*, 8089-8099.

25. Xie, S.; Liu, X. Y.; Xia, Y., Shape-Controlled Syntheses of Rhodium Nanocrystals for the Enhancement of Their Catalytic Properties. *Nano Res.* **2015**, *8*, 82-96.

26. Zhang, H.; Li, W.; Jin, M.; Zeng, J.; Yu, T.; Yang, D.; Xia, Y., Controlling the Morphology of Rhodium Nanocrystals by Manipulating the Growth Kinetics with a Syringe Pump. *Nano Lett*. **2011**, *11*, 898-903.

27. Humphrey, S. M.; Grass, M. E.; Habas, S. E.; Niesz, K.; Somorjai, G. A.; Tilley, T. D., Rhodium Nanoparticles from Cluster Seeds: Control of Size and Shape by Precursor Addition Rate. *Nano Lett.* **2007**, *7*, 785-790.

28. Yu, N. F.; Tian, N.; Zhou, Z. Y.; Huang, L.; Xiao, J.; Wen, Y. H.; Sun, S. G., Electrochemical Synthesis of Tetrahexahedral Rhodium Nanocrystals with Extraordinarily High Surface Energy and High Electrocatalytic Activity. *Angew. Chem. Int. Ed.* **2014**, *53*, 5097-5101.

29. Thostrup, P.; Christoffersen, E.; Lorensen, H.; Jacobsen, K. W.; Besenbacher, F.; Nørskov, J. K., Adsorption-Induced Step Formation. *Phys. Rev. Lett.* **2001**, *87*, 126102.

30. Tao, F. F.; Crozier, P. A., Atomic-Scale Observations of Catalyst Structures under Reaction Conditions and During Catalysis. *Chem. Rev.* **2016**, *116*, 3487-539.

31. Zhou, Y.; Jin, C.; Li, Y.; Shen, W., Dynamic Behavior of Metal Nanoparticles for Catalysis. *Nano Today*. **2018**, *20*, 101-120.

32. Tao, F. F.; Nguyen, L.; Zhang, S.; Li, Y.; Tang, Y.; Zhang, L.; Frenkel, A. I.; Xia, Y.; Salmeron, M., Formation of Second-Generation Nanoclusters on Metal Nanoparticles Driven by Reactant Gases. *Nano lett.* **2016**, *16*, 5001-5009.

33. Hansen, P. L.; Wagner, J. B.; Helveg, S.; Rostrup-Nielsen, J. R.; Clausen, B. S.; Topsøe, H., Atom-Resolved Imaging of Dynamic Shape Changes in Supported Copper Nanocrystals. *Science*. **2002**, *295*, 2053-2055.

34. Duan, M.; Yu, J.; Meng, J.; Zhu, B.; Wang, Y.; Gao, Y., Reconstruction of Supported Metal Nanoparticles in Reaction Conditions. *Angew. Chem. Int. Ed.* **2018**, *130*, 6574-6579.

35. Chmielewski, A.; Meng, J.; Zhu, B.; Gao, Y.; Guesmi, H.; Prunier, H.; Alloyeau, D.; Wang, G.; Louis, C.; Delannoy, L., Reshaping Dynamics of Gold Nanoparticles under H_2 and O_2 at Atmospheric Pressure. *ACS Nano*. **2019**, *13*, 2024-2033.

36. Altantzis, T.; Lobato, I.; De Backer, A.; Béché, A.; Zhang, Y.; Basak, S.; Porcu, M.; Xu, Q.; Sánchez Iglesias, A.; Liz Marzán, L. M., Three-Dimensional Quantification of the Facet Evolution of Pt Nanoparticles in a Variable Gaseous Environment. *Nano Lett.* **2018**, *19*, 477-481.

37. Cabié, M.; Giorgio, S.; Henry, C. R.; Axet, M. R.; Philippot, K.; Chaudret, B., Direct Observation of the Reversible Changes of the Morphology of Pt Nanoparticles under Gas Environment. *J. Phys. Chem. C*. **2010**, *114*, 2160-2163.

38. Vendelbo, S. B., et al., Visualization of Oscillatory Behaviour of Pt Nanoparticles Catalysing CO Oxidation. *Nat. Mater.* **2014**, *13*, 884-890.

39. Anic, K.; Bukhtiyarov, A. V.; Li, H.; Rameshan, C.; Rupprechter, G., CO Adsorption on Reconstructed Ir(100) Surfaces from UHV to mbar Pressure: A LEED, TPD, and PM-IRAS Study. *J. Phys. Chem. C*. **2016**, *120*, 10838-10848.

40. Zhang, X.; Meng, J.; Zhu, B.; Yuan, W.; Yang, H.; Zhang, Z.; Gao, Y.; Wang, Y., Unexpected Refacetting of Palladium Nanoparticles under Atmospheric N_2 Conditions. *Chem. Commun.* **2018**, *54*, 8587-8590.

41. Rossi, K.; Asara, G. G.; Baletto, F., A Genomic Characterisation of Monometallic Nanoparticles. *Phys. Chem. Chem. Phys.* **2019**, *21*, 4888-4898.
42. Brodersen, S. H.; Grønbjerg, U.; Hvolbæk, B.; Schiøtz, J., Understanding the Catalytic Activity of Gold Nanoparticles through Multi-Scale Simulations. *J. Catal.* **2011**, *284*, 34-41.
43. Li, X. Y.; Zhu, B.; Qi, R.; Gao, Y., Real-Time Simulation of Nonequilibrium Nanocrystal Transformations. *Adv. Theor. Simul.* **2019**, *2*, 1800127.
44. Turner, C. H.; Lei, Y.; Bao, Y., Modeling the Atomistic Growth Behavior of Gold Nanoparticles in Solution. *Nanoscale*. **2016**, *8*, 9354-9365.
45. Chepkasov, I. V.; Visotin, M. A.; Kovaleva, E. A.; Manakhov, A. M.; Baidyshev, V. S.; Popov, Z. I., Stability and Electronic Properties of PtPd Nanoparticles Via MD and DFT Calculations. *J. Phys. Chem. C*. **2018**, *122*, 18070-18076.
46. Kim, H. Y.; Hybertsen, M. S.; Liu, P., Controlled Growth of Ceria Nanoarrays on Anatase Titania Powder: A Bottom-up Physical Picture. *Nano Lett.* **2017**, *17*, 348-354.
47. Nanba, Y.; Ishimoto, T.; Koyama, M., Structural Stability of Ruthenium Nanoparticles: A Density Functional Theory Study. *J. Phys. Chem. C.* **2017**, *121*, 27445-27452.
48. An, W.; Liu, P., Rationalization of Au Concentration and Distribution in AuNi@Pt Core–Shell Nanoparticles for Oxygen Reduction Reaction. *ACS Catal.* **2015**, *5*, 6328-6336.
49. An, W.; Liu, P., Size and Shape Effects of Pd@Pt Core–Shell Nanoparticles: Unique Role of Surface Contraction and Local Structural Flexibility. *J. Phys. Chem. C*. **2013**, *117*, 16144-16149.
50. Du, J.; Meng, J.; Li, X.-Y.; Zhu, B.; Gao, Y., Multiscale Atomistic Simulation of Metal Nanoparticles under Working Conditions. *Nanoscale Adv.* **2019**, *1*, 2478-2484.
51. Zhu, B.; Xu, Z.; Wang, C.; Gao, Y., Shape Evolution of Metal Nanoparticles in Water Vapor Environment. *Nano Lett.* **2016**, *16*, 2628-2632.
52. Xu, L.; Liang, H. W.; Yang, Y.; Yu, S. H., Stability and Reactivity: Positive and Negative Aspects for Nanoparticle Processing. *Chem. Rev.* **2018**, *118*, 3209-3250.
53. Zeng, X.; Huang, R.; Wen, Y.; Sun, S., Thermal and Shape Stability of High-Index-Faceted Rhodium Nanoparticles: A Molecular Dynamics Investigation. *Phys. Chem. Chem. Phys.* **2015**, *17*, 5751-5757.
54. Ellaby, T.; Aarons, J.; Varambhia, A.; Jones, L.; Nellist, P.; Ozkaya, D.; Sarwar, M.; Thompsett, D.; Skylaris, C., Ideal Versus Real: Simulated Annealing of Experimentally Derived and Geometric Platinum Nanoparticles. *J. Phys.: Condens. Matter*. **2018**, *30*, 155301.
55. Huang, R.; Wen, Y. H.; Shao, G. F.; Zhu, Z. Z.; Sun, S. G., Thermal Stability and Shape Evolution of Tetrahexahedral Au–Pd Core–Shell Nanoparticles with High-Index Facets. *J. Phys. Chem. C*. **2013**, *117*, 6896–6903.
56. An, W., The Role of Synergic Interaction in Transition State Formation for the Aldol Reaction on a Metal Oxide Catalyst: A DFT Investigation. *Phys. Chem. Chem. Phys.* **2015**, *17*, 22529-22532.
57. Barmparis, G. D.; Remediakis, I. N., Dependence on CO Adsorption of the Shapes of Multifaceted Gold Nanoparticles: A Density Functional Theory. *Phys. Rev. B*. **2012**, *86*, 085457.
58. Limmer, D. T.; Willard, A. P.; Madden, P.; Chandler, D., Hydration of Metal Surfaces Can Be Dynamically Heterogeneous and Hydrophobic. *Proc. Natl. Acad. Sci.* **2013**, *110*, 4200-4205.
59. Carrasco, J.; Hodgson, A.; Michaelides, A., A Molecular Perspective of Water at Metal Interfaces. *Nat. Mater.* **2012**, *11*, 667-674.
60. Hodgson, A.; Haq, S., Water Adsorption and the Wetting of Metal Surfaces. *Surf. Sci. Rep.* **2009**, *64*, 381-451.
61. Doi: https://doi.org/10.18434/T4D303.
62. Wang, H.; An, W., Promoting the Oxygen Reduction Reaction with Gold at Step/Edge Sites of Ni@AuPt Core–Shell Nanoparticles. *Catal. Sci. Technol.* **2017**, *7*, 596-606.
63. Kresse, G.; Furthmüller, J., Efficient Iterative Schemes for Ab Initio Total-Energy Calculations Using a Plane-Wave Basis

Set. *Phys. Rev. B*. **1996**, *54*, 11169-11186.

64. Kresse, G.; Joubert, D., From Ultrasoft Pseudopotentials to the Projector Augmented-Wave Method. *Phys. Rev. B*. **1999**, *59*, 1758-1775.

65. Perdew, J. P.; Chevary, J. A.; Vosko, S. H.; Jackson, K. A.; Pederson, M. R.; Singh, D. J.; Fiolhais, C., Atoms, Molecules, Solids, and Surfaces: Applications of the Generalized Gradient Approximation for Exchange and Correlation. *Phys. Rev. B*. **1992**, *46*, 6671-6687.

66. Monkhorst, H. J.; Pack, J. D., Special Points for Brillouin-Zone Integrations. *Phys. Rev. B*. **1976**, *13*, 5188-5192.

67. Fiorentini, V.; Methfessel, M., Extracting Convergent Surface Energies from Slab Calculations. *J. Phys.: Condens. Matter*. **1996**, *8*, 6525-6529.

68. Klimeš, J.; Bowler, D. R.; Michaelides, A., Van Der Waals Density Functionals Applied to Solids. *Phys. Rev. B*. **2011**, *83*, 195131.

69. Plimpton, S., Fast Parallel Algorithms for Short-Range Molecular Dynamics. *J. Comput. Phys*. **1995**, *117*, 1-19.

70. Sheng, H.; Kramer, M.; Cadien, A.; Fujita, T.; Chen, M., Highly Optimized Embedded-Atom-Method Potentials for Fourteen Fcc Metals. *Phys. Rev. B*. **2011**, *83*, 134118.

71. Hoover, W. G., Canonical Dynamics: Equilibrium Phase-Space Distributions. *J. Phys. A: Gen. Phys.* **1985**, *31*, 1695.

72. Stukowski, A., Visualization and Analysis of Atomistic Simulation Data with OVITO–the Open Visualization Tool. *Modell. Simul. Mater. Sci. Eng.* **2009**, *18*, 015012.

73. Cleveland, C. L.; Landman, U.; Schaaff, T. G.; Shafigullin, M. N.; Stephens, P. W.; Whetten, R. L., Structural Evolution of Smaller Gold Nanocrystals: The Truncated Decahedral Motif. *Phys. Rev. Lett.* **1997**, *79*, 1873-1876.

74. Ligthart, D. A.; van Santen, R. A.; Hensen, E. J., Supported Rhodium Oxide Nanoparticles as Highly Active CO Oxidation Catalysts. *Angew. Chem. Int. Ed. Engl.* **2011**, *50*, 5306-5310.

75. Berkó, A.; Ménesi, G.; Solymosi, F., STM Study of Rhodium Deposition on the TiO_2(110)-(1×2) Surface. *Surf. Sci.* **1997**, *372*, 202-210.

76. Berkó, A.; Solymosi, F., Effects of Different Gases on the Morphology of Ir Nanoparticles Supported on the TiO_2 (110)-(1×2) Surface. *J. Phys. Chem. B*. **2000**, *104*, 10215-10221.

77. Cabié, M.; Giorgio, S.; Henry, C. R.; Axet, M. R.; Philippot, K.; Chaudret, B., Direct Observation of the Reversible Changes of the Morphology of Pt Nanoparticles under Gas Environment. *J. Phys. Chem. C.* **2010**, *114*, 2160-2163.

78. Zhang, Y.; Pluchery, O.; Caillard, L.; Lamic-Humblot, A. F.; Casale, S.; Chabal, Y. J.; Salmeron, M., Sensing the Charge State of Single Gold Nanoparticles Via Work Function Measurements. *Nano Lett.* **2015**, *15*, 51-55.

79. Wang, P.; Tanaka, D.; Ryuzaki, S.; Araki, S.; Okamoto, K.; Tamada, K., Silver Nanoparticles with Tunable Work Functions. *Appl. Phys. Lett.* **2015**, *107*, 151601.

TOC Graphic

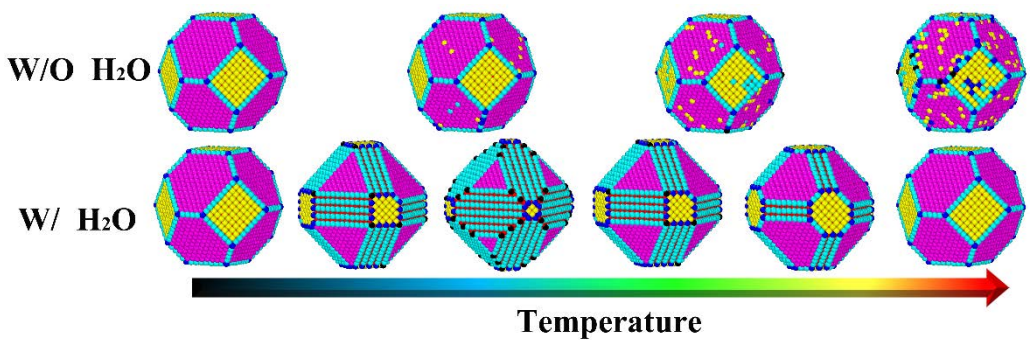

Probing Structural Reconstruction of Metal Nanoparticles under Annealing and Water Vapor Conditions: A Theoretical Study

Zeming Wang,[†] Wei An,[*,†], Yangang Sun,[†] Mark S. Hybertsen[‡]

[†]College of Chemistry and Chemical Engineering, Shanghai University of Engineering Science, Songjiang District, Shanghai 201620, China

[‡]Center for Functional Nanomaterials, Brookhaven National Laboratory, Upton, New York 11973, United States

*E-mail: weian@sues.edu.cn

Table S1. Surface tension (γ_{hkl}), atomic area (A_{at}), and work function (Φ) of low-index facets of Rh and Ir along with adsorption energy (E_{ads}) of H_2O.

Metal	Facets	γ_{hkl} (eV/Å^2)		A_{at} (Å^2)	Φ(eV)	E_{ads} (eV)	
		This work	Ref.[a]	This work	Ref.[b]	This work	Ref.
Rh	(111)	0.121	0.124	6.27	5.17	-0.49	-0.44[c]
	(100)	0.142	0.145	7.24	5.00	-0.49	-
	(110)	0.145	0.145	10.23	4.65	-0.65(-0.57)[e]	-
Ir	(111)	0.149	0.143	6.49	5.59	-0.52	-0.49[d]
	(100)	0.181	0.176	7.50	5.47	-0.57	-
	(110)	0.183	0.177	10.60	5.04	-0.74(-0.66)[e]	-

[a] See Ref. 1.
[b] See Ref. 2.
[c] See Ref. 3.
[d] See Ref. 4.
[e] Adsorption energy of H_2O at edges site of (221) surface listed in parentheses.

Table S2. Potential binding energy (BE)* of bulk metals under annealing temperature of 300 K-900 K.

	BE (eV/atom)			
Metal	300 K	500 K	700 K	900 K
Rh	-5.711	-5.683	-5.653	-5.622
Ir	-6.901	-6.875	-6.848	-6.820

*DFT-calculated BE: Rh = -7.33 eV/atom; Ir = -8.86 eV/atom.

Table S3. The surface atomic concentrations of 5.5-nm Rh and Ir NPs ($\overline{CN}$ = 7.2, 7.5, 7.8, 8.2, 8.5) under water vapor conditions.

Metal	Sites	$\overline{CN}$ of NPs				
		7.2	7.5	7.8	8.2	8.5
Rh	(111)	0.15	0.27	**0.38**	**0.55**	0.66
	(100)	0.03	0.07	**0.12**	**0.15**	0.19
	(110)	0.73	0.58	**0.43**	**0.25**	0.14
	Edge	0.04	0.06	**0.06**	**0.05**	0.01
	Corner	0.05	0.02	**0.01**	**0.00**	0.01
Ir	(111)	0.15	0.27	**0.28**	**0.48**	0.66
	(100)	0.03	0.07	**0.24**	**0.28**	0.19
	(110)	0.73	0.58	**0.33**	**0.19**	0.14
	Edge	0.04	0.06	**0.09**	**0.05**	0.01
	Corner	0.05	0.02	**0.00**	**0.00**	0.01

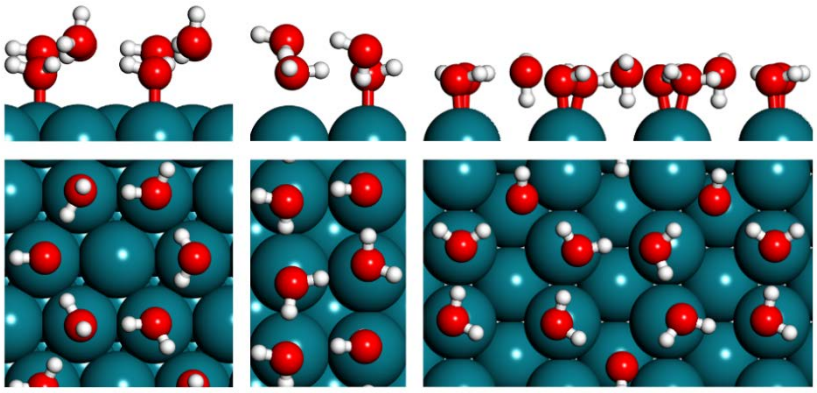

(111) (100) (110)

Figure S1. DFT-optimized structures for the full-coverage of H_2O adsorbed on (110), (100) and (111) facets of Rh, which correspond to θ_{ML} = 0.67, 1.0 and 0.67, respectively. Same as Ir.

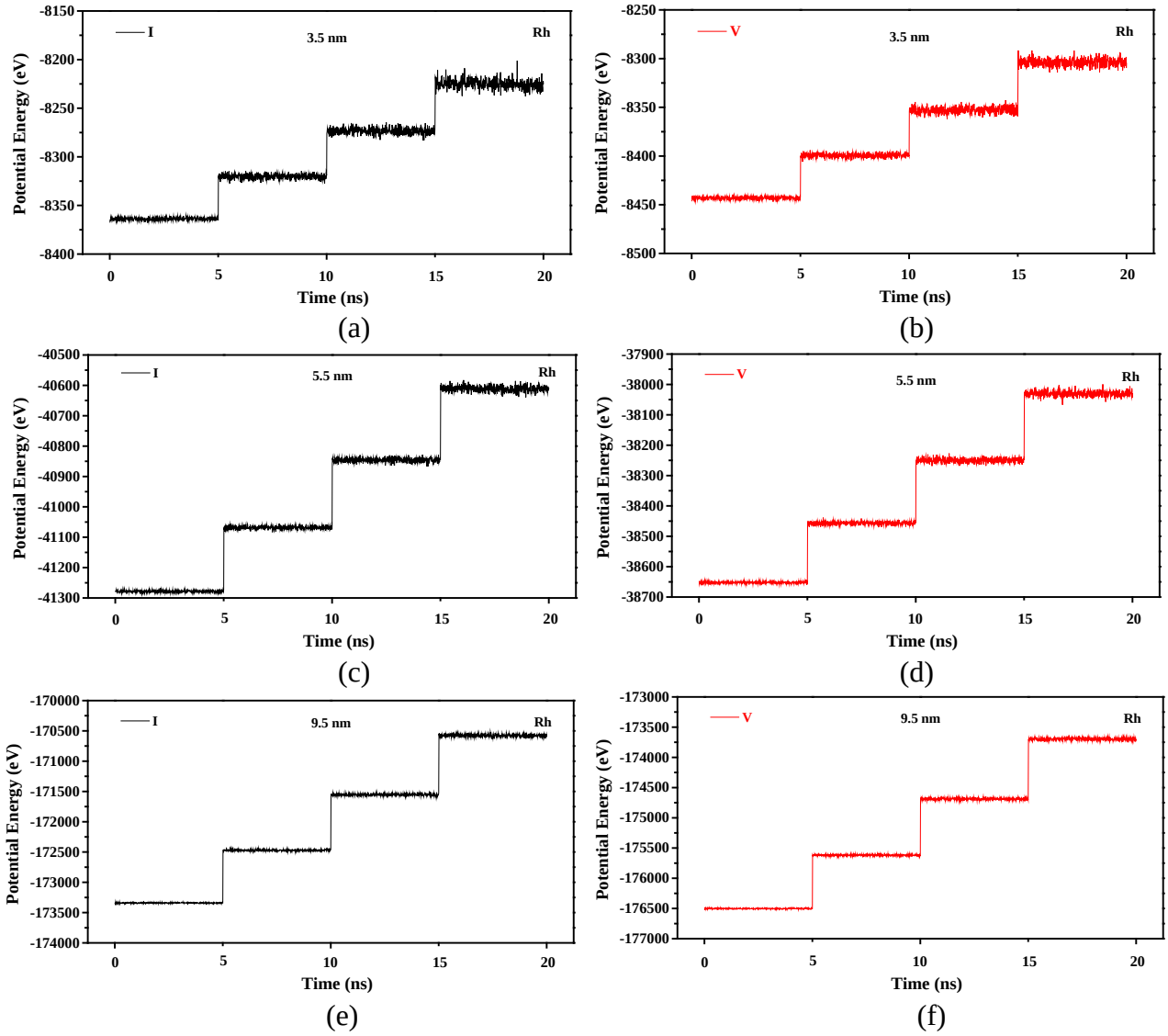

Figure S2. Potential energy fluctuations with time progress and elevated temperature in MD simulations of annealing of Rh NPs (3.5 nm, 5.5nm, and 9.5 nm). Left panel: **I**. Right panel: **V**. 300 K: 0 ns - 5 ns; 500 K: 5 ns - 10 ns; 700 K: 10 ns - 15 ns; 900 K: 15 ns - 20 ns.

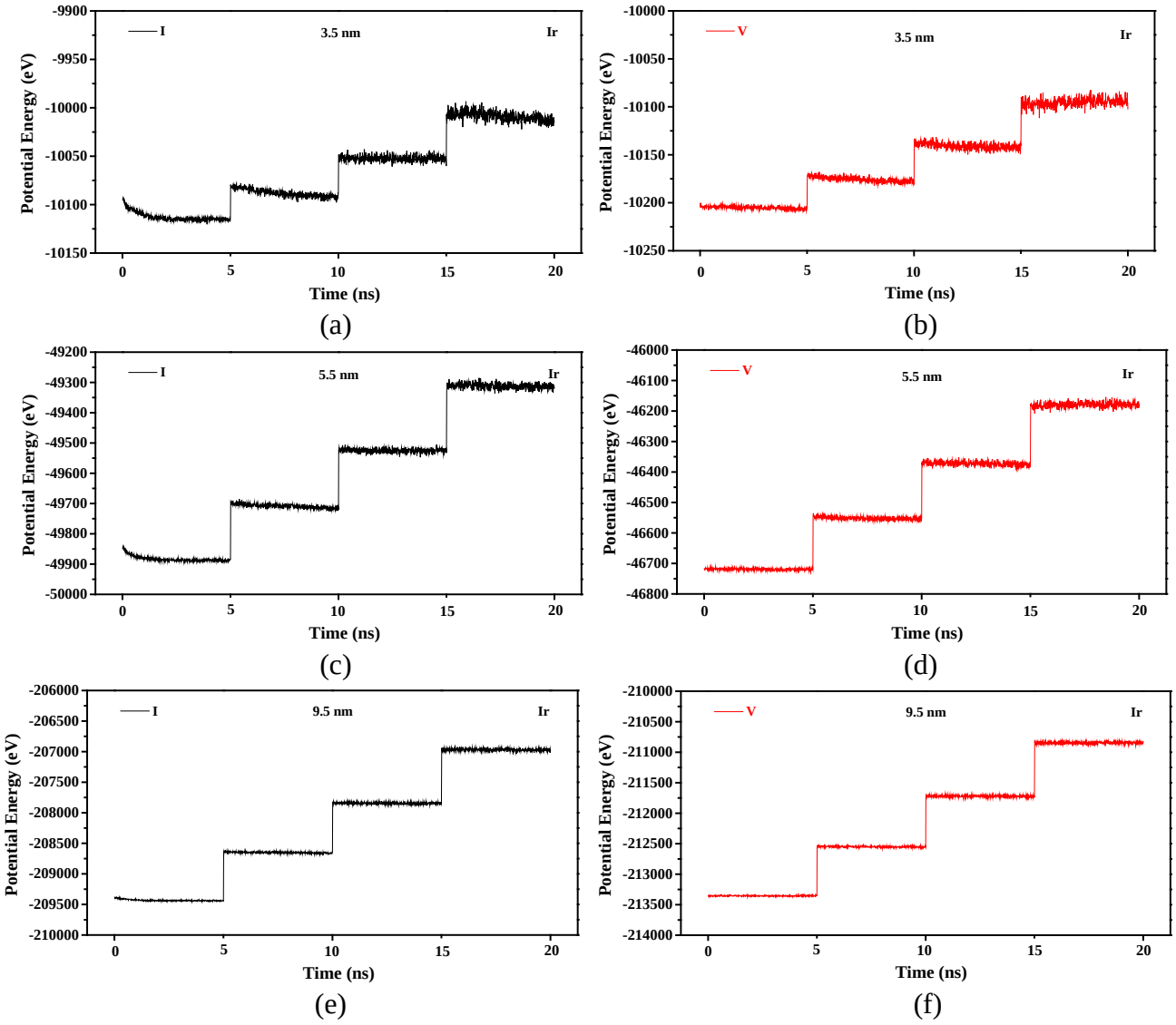

Figure S3. Potential energy fluctuations with time progress and elevated temperature in MD simulations of annealing of Ir NPs (3.5 nm, 5.5nm, and 9.5 nm). Left panel: **I**. Right panel: **V**. 300 K: 0 ns - 5 ns; 500 K: 5 ns - 10 ns; 700 K: 10 ns - 15 ns; 900 K: 15 ns - 20 ns.

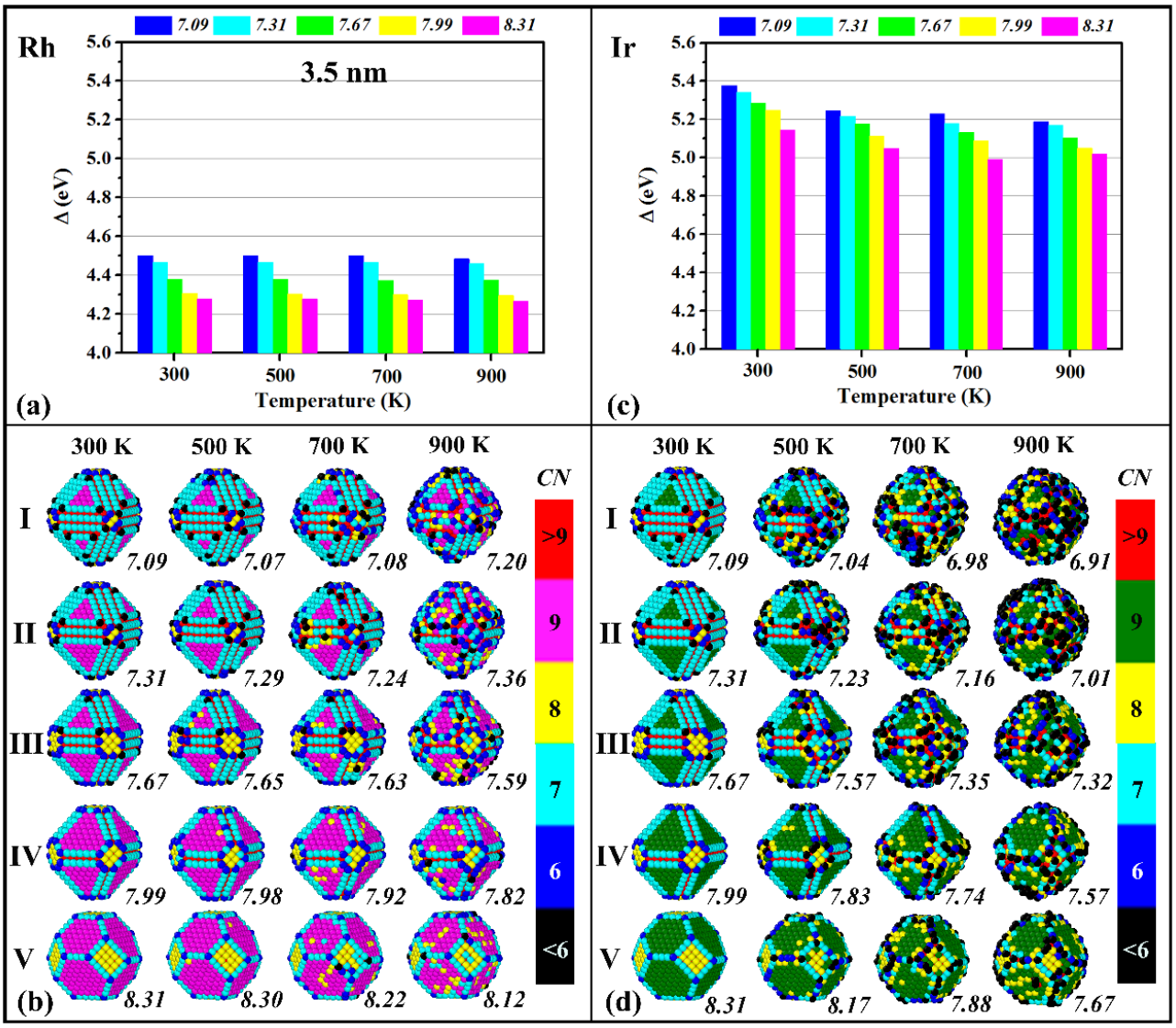

Figure S4. Thermal stability and structural reconstruction of metal nanoparticles (d = 3.5 nm) with increased temperature. Rh: (a) structural transformation inertness (Δ), (b) snapshot; Ir: (c) structural transformation inertness (Δ), (d) snapshot.

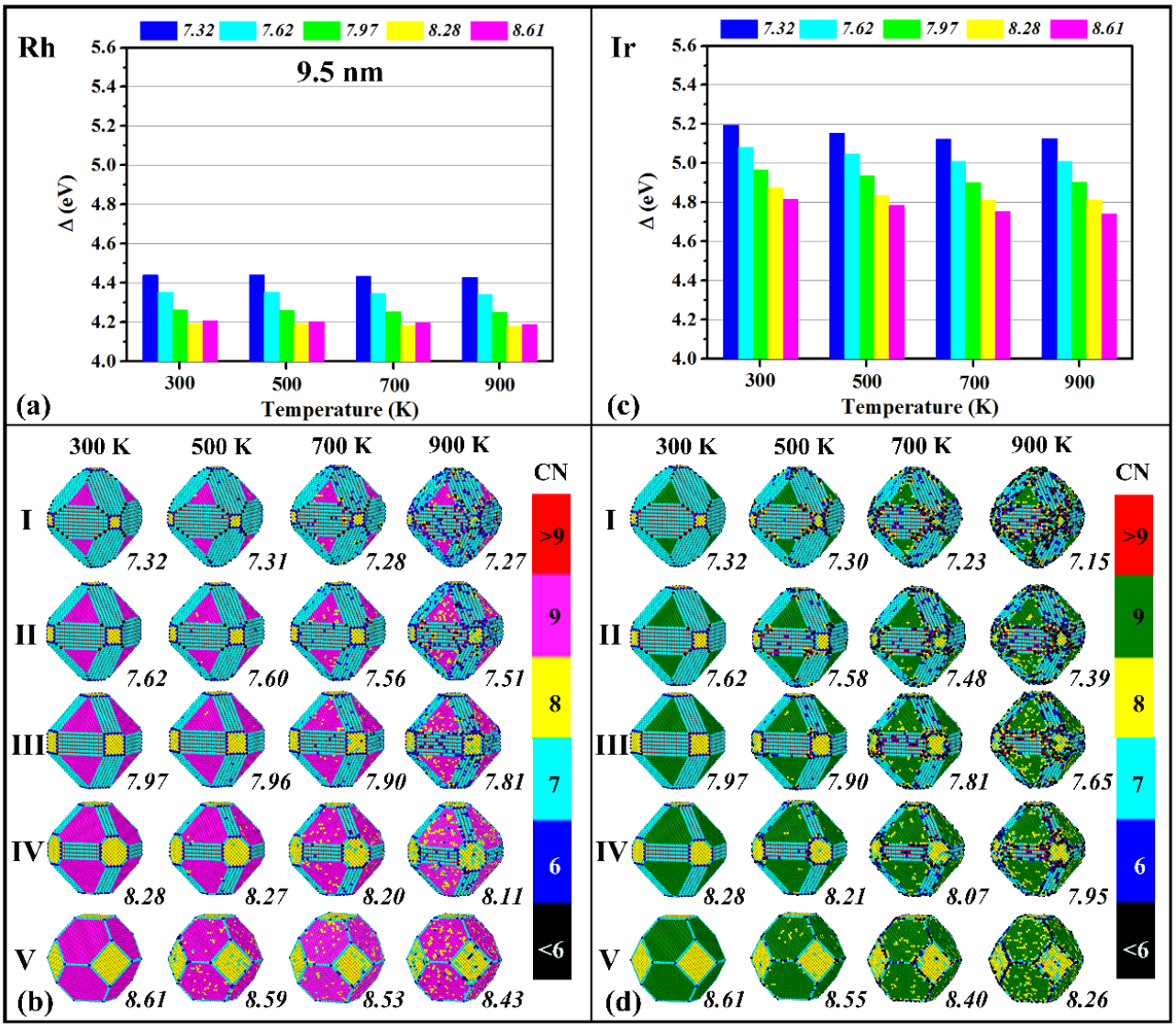

Figure S5. Thermal stability and structural reconstruction of metal nanoparticles (d = 9.5 nm) with increased temperature. Rh: (a) structural transformation inertness (Δ), (b) snapshot; Ir: (c) structural transformation inertness (Δ), (d) snapshot.

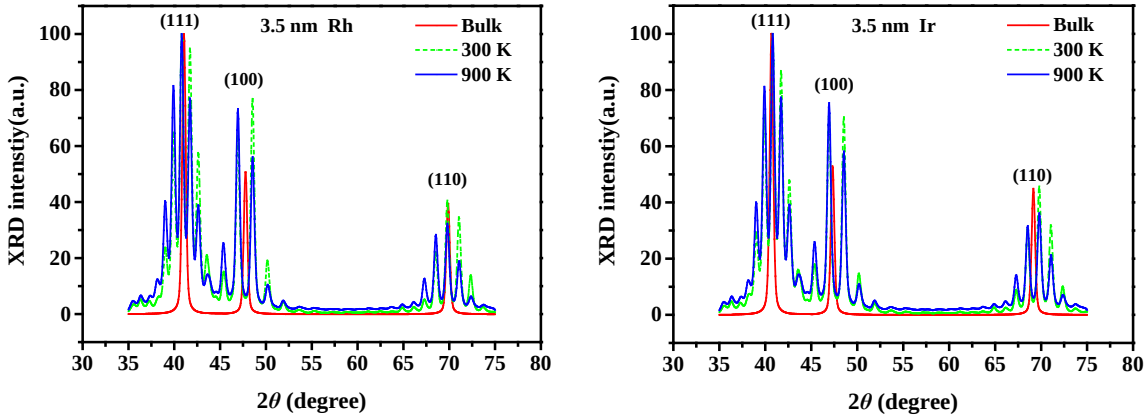

(a) (b)

Figure S6. Simulated XRD spectra of bulk structure and **I** structure of 3.5nm NP. (a) Rh and (b) Ir. Simulated XRD spectra were obtained using Reflex module embedded in Materials Studio 7.0 with the parameters: $Cu_{\alpha}(\lambda)$ = 1.5406 Å, step size= 0.05° and Pseudo-Voigt broadening of 0.1°.

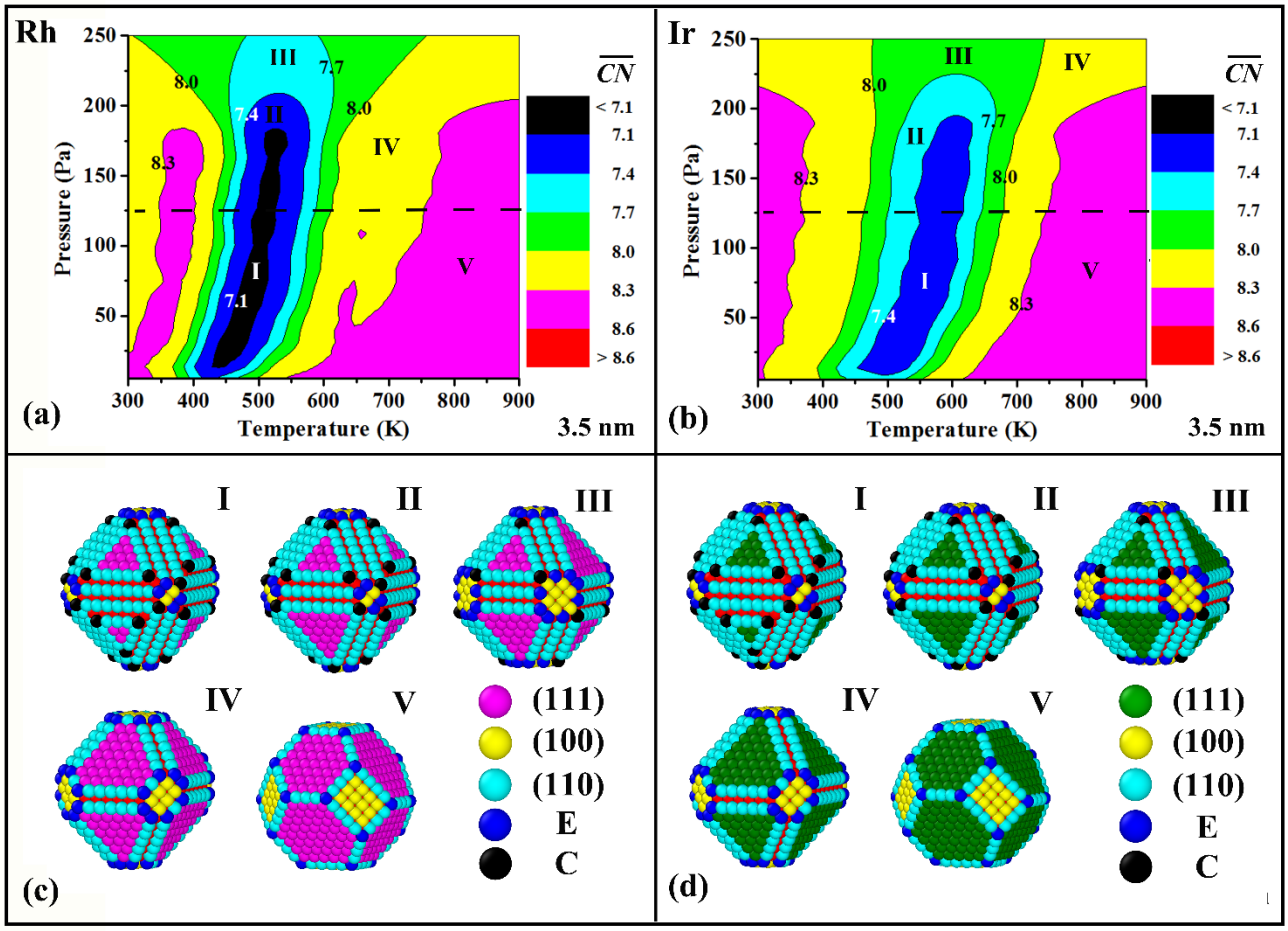

Figure S7. Structural isosurface ($\overline{CN}$) of 3.5-nm NPs of (a) Rh and (b) Ir as functions of temperature and pressure of water vapor. Representative NP structures (**I - V**) of (c) Rh and (d) Ir corresponding to five typical regions (with the matched color). Black dashed line: at 125 Pa.

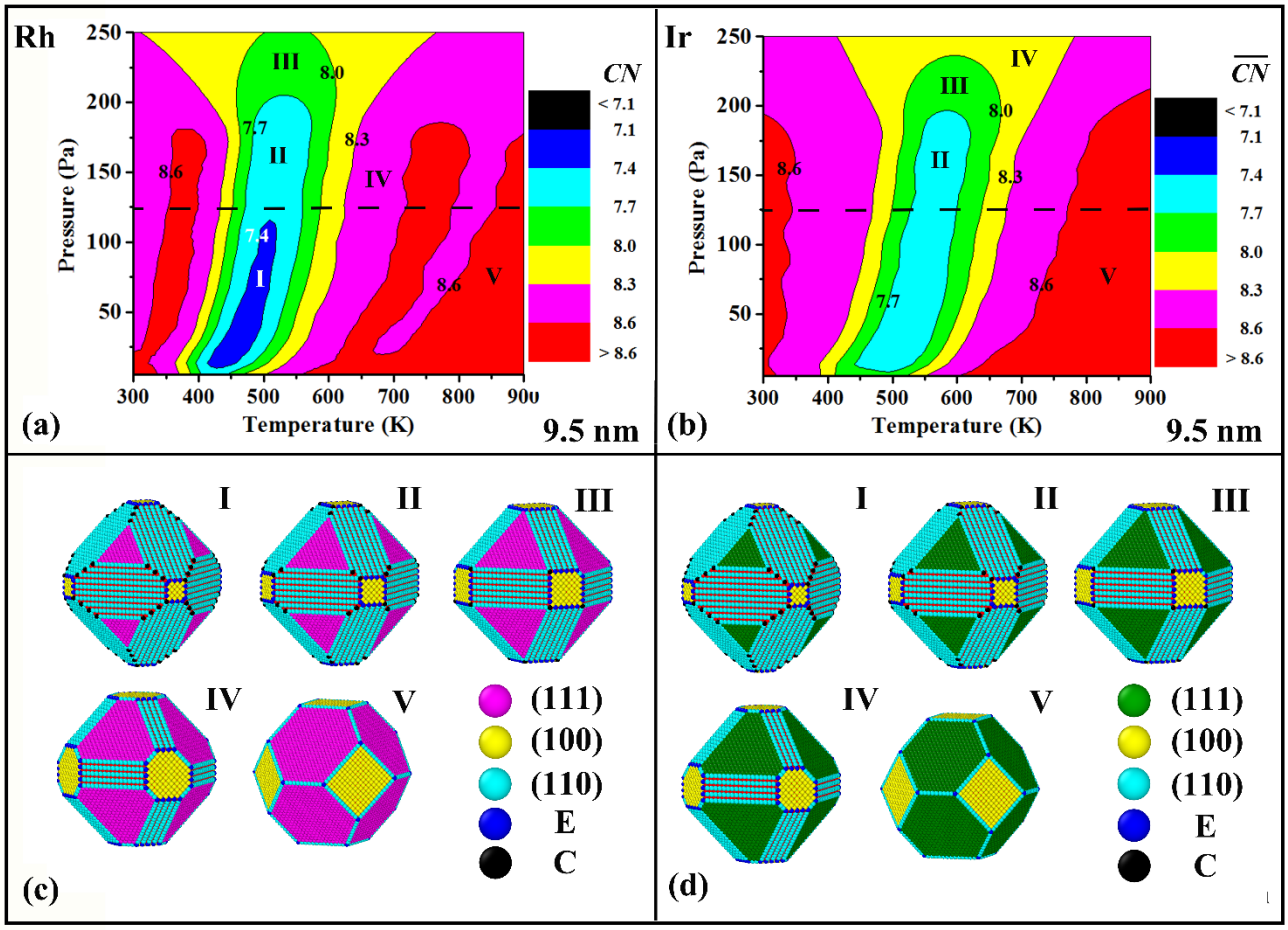

Figure S8. Structural isosurface ($\overline{CN}$) of 9.5-nm NPs of (a) Rh and (b) Ir as functions of temperature and pressure of water vapor. Representative NP structures (**I - V**) of (c) Rh and (d) Ir corresponding to five typical regions (with the matched color). Black dashed line: at 125 Pa.

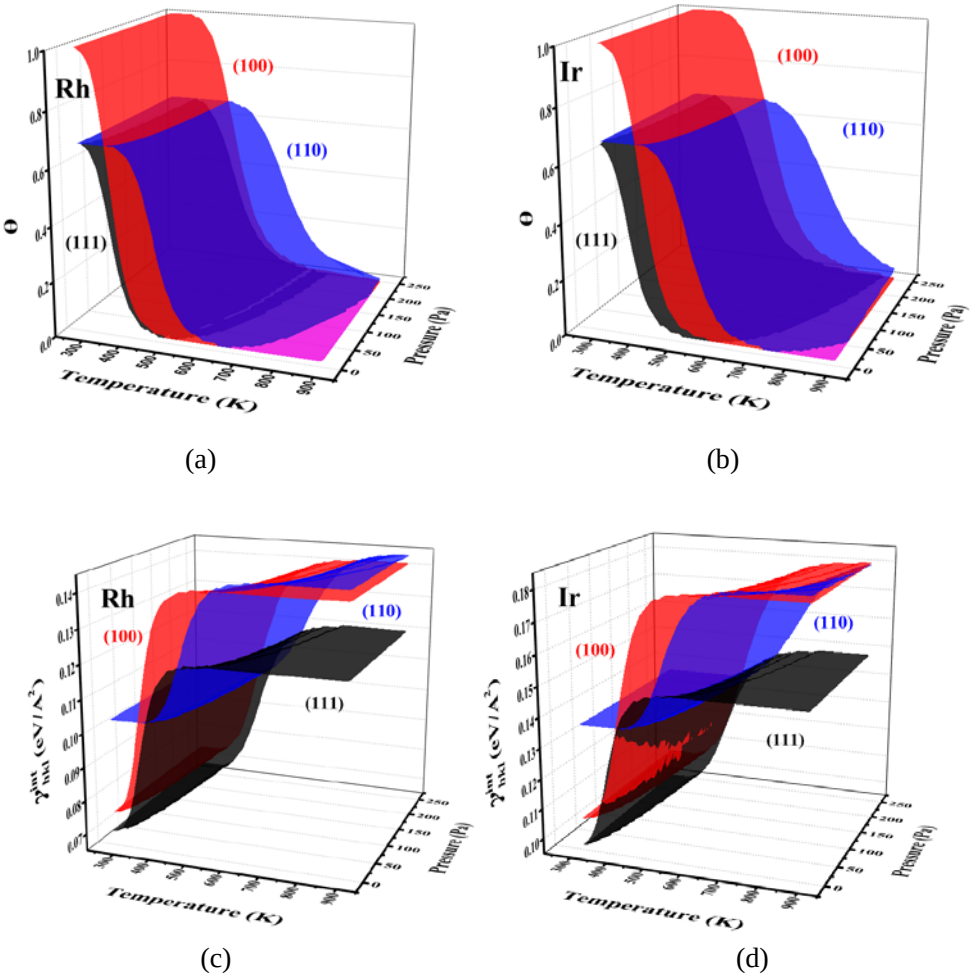

(a) (b)

(c) (d)

Figure S9. Three-dimensional contour of H_2O coverage (a) (b) and interfacial tension (c) (d) on different facets of 5.5 nm Rh and Ir NPs as a function of temperature and pressure of water vapor. Black: (111) facets; Red: (100) facets; Blue: (110) facets.

REFERENCES

1. Tran, R.; Xu, Z.; Radhakrishnan, B.; Winston, D.; Sun, W.; Persson, K. A.; Ong, S. P., Surface Energies of Elemental Crystals. *Sci. Data*. **2016**, *3*, 160080.
2. Tran, R.; Li, X.-G.; Montoya, J. H.; Winston, D.; Persson, K. A.; Ong, S. P., Anisotropic Work Function of Elemental Crystals. *Surf. Sci.* **2019**, *687*, 48-55.
3. Carrasco, J.; Klimeš, J.; Michaelides, A., The Role of Van Der Waals Forces in Water Adsorption on Metals. *J. Chem. Phys.* **2013**, *138*, 024708.
4. Karlberg, G., Adsorption Trends for Water, Hydroxyl, Oxygen, and Hydrogen on Transition-Metal and Platinum-Skin Surfaces. *Phys. Rev. B*. **2006**, *74*, 153414.